

Atomic Engineering on 2D Materials using Electron Irradiation and Chemical Protection

By

Cong Su

B.S., Applied Physics (2013), Yuanpei College, Peking University

SUBMITTED TO THE
DEPARTMENT OF NUCLEAR SCIENCE AND ENGINEERING
IN PARTIAL FULFILLMENT OF THE REQUIREMENTS FOR THE DEGREE OF
DOCTOR OF PHILOSOPHY IN NUCLEAR SCIENCE AND ENGINEERING

AT THE
MASSACHUSETTS INSTITUTE OF TECHNOLOGY
February, 2020

© 2020 Massachusetts Institute of Technology
All rights reserved.

Signature of Author: _____
Cong Su
Department of Nuclear Science and Engineering
September 30, 2019

Certified by: _____
Ju Li
Battelle Energy Alliance Professor of Nuclear Science and Engineering and Professor of
Materials Science and Engineering
Thesis Advisor

Certified by: _____
Jing Kong
Professor of Electrical Engineering and Computer Science
Thesis Advisor

Certified by: _____
Paola Cappellaro
Esther and Harold E. Edgerton Associate Professor of Nuclear Science and Engineering
Thesis Reader

Certified by: _____
Juan-Carlos Idrobo
Staff Scientist at Oak Ridge National Laboratory and Adjunct Professor of Materials Science and
Engineering in Vanderbilt University
Thesis Committee Member

Accepted by: _____
Ju Li
Battelle Energy Alliance Professor of Nuclear Science and Engineering and Professor of
Materials Science and Engineering
Chair, Department Committee on Graduate Students

Atomic Engineering on 2D Materials using Electron Irradiation and Chemical Protection

by

Cong Su

Submitted to the Department of Nuclear Science and Engineering
on Oct. 3, 2019, in partial fulfillment of the requirements for the degree of
Doctor of Philosophy

Abstract

Controlling the exact atomic structure is an ultimate form of engineering. Atomic manipulation and atom-by-atom assembly can create functional structures that are hard to synthesize chemically. Defects with one- or few-atom-scale pertain intriguing properties that can be applicable to fields like Quantum Engineering (e.g. nitrogen vacancy center, single photon emitter, etc.), or Single-Atom Catalysis. Historically, scanning tunneling microscopy (STM) has demonstrated good stepwise control of single atoms, leading to physicochemical insights and technological advances. However, their scalability and throughput are severely limited by the mechanical probe movements, and its applicability is constrained by the low-temperature environment (usually lower than 77K) needed for stabilize the structure. Therefore, a method of controlling atoms at room-temperature without mechanical movement is essential for a broader interest and unleashing the constraints. The advancement of aberration corrector makes it possible to focus high-energy (usually ranging from 30 keV to 300 keV) electron beams to a single-atom scale inside scanning transmission electron microscope (STEM). Despite being a versatile tool for characterizing the precise atomic structures of materials, STEM has also demonstrated the capability of controlling atoms on two-dimensional (2D) materials, like a substitutional dopant in graphene or molybdenum disulfides (MoS_2). This turns the irradiation damage of electron beam (which is not what we want) to a powerful tool with a positive value (what we want). While controlling atoms using STEM is promising, it is still haunted by the fact that most of the dynamic processes are random.

The core of this thesis, a theoretical framework called Primary Knock-on Space (PKS), will be introduced for optimizing the control process by biasing the possibilities of different atomic dynamics. This framework predicts how various external factors tunable in experiment, such as temperature, electron beam incident angle, electron beam voltage, and dopant species, can influence the atom dynamics. It is proved to be useful in guiding the control process towards a more deterministic route. Following the introduction of the framework, several proof-of-concept experiments are demonstrated for validating the PKS framework. The future of Atomic Engineering will also be envisioned at the end. An additional corrosion inhibition of 2D materials will also be discussed, which is found to be critical during the materials transfer process.

Thesis Advisor: Ju Li

Title: Battelle Energy Alliance Professor of Nuclear Science and Engineering and Professor of Materials Science and Engineering

Thesis Advisor: Jing Kong

Title: Professor of Electrical Engineering and Computer Science

Thesis Reader: Paola Cappellaro

Title: Esther and Harold E. Edgerton Associate Professor of Nuclear Science and Engineering

Thesis Committee Member: Juan-Carlos Idrobo

Title: Staff Scientist at Oak Ridge National Laboratory and Adjunct Professor of Materials Science and Engineering in Vanderbilt University

Acknowledgments

Six years are a *long* time, and it is hard to believe that I have already been in MIT for more than the period of my middle school and high school combined. Six years are also *short*, as I can still clearly remember the very first day when I came to MIT, and recall my thrill when I stepped into a land of wonder. Ph.D. program is *hard*, in the sense that there are a lot more uncertainties than I expected. It is also *easy*, thanks to the support of all the people who helped me with their extraordinary expertise while I was struggling on my way. It is these fantastic individuals I met that really helped form the shape of this thesis that you are reading here.

After my first year enjoying my life with a bunch of courses that I deemed to be not *that* hard, I was assigned by Prof. Ju Li with a clear simple task: “try moving atoms”. For one thing, he told me that atomic-level fabrication is clearly a trend after the hype of nano engineering, where human instinct is to pursue a technique with increasingly higher precision. For the other, I was told that I am obliged to contribute to nuclear engineering as I’m officially affiliated under NSE, so that the project, “elastic strain engineering” I was initially assigned, sounds like a peripheral project that I can barely contribute a substantial amount of knowledge to nuclear science. I was convinced. The very first few months was a real struggle: I had zero knowledge about how to move atoms, nor did I know any technique I can use for moving atoms. The only thing I remembered at that time was a picture with “IBM” logo appeared on my high school textbook.

One day, there was one paper published on Physical Review Letters that caught my attention. It was a newly published paper talking about the a dopant atom exchanging its site with the neighbor carbon atom when they are scanned by high energy electron beam. That was such a eureka moment and I realized that it is exactly what I’m looking for. The technique seems to be able to control atoms, and the electron irradiation effect had been taught in the course. There were two problems I was facing though: 1. I don’t know where I can get the doped graphene sample to start with; 2. To complete this experiment, I need to use high-end electron

microscope equipped with aberration corrector. Harvard has one, but it was a TEM which is not specialized to focus electron into a small probe. I didn't know where I can find the proper machine for looking at the atoms, let alone moving them.

To solve my first problem, I found Prof. Jing Kong, who later became my co-advisor in Ph.D. thesis, and one of my most important mentors in my career path. Jing has a very soft voice and was willing to give me advice on how I can get my samples. But she warned me the risk of this project, and kindly suggested me focus on the qualification exam before anything else should be discussed further. As a final remark, Jing asked me to meet with Prof. Mildred Dresselhaus for some advice. Mille, also been known as the "Queen of Carbon", was reluctant to encourage me to keep on this project after patiently listening to my ten-minute soliciting and bragging about this project. But luckily, she agreed to become my thesis committee member and told me to "come and find her if it doesn't work out well". She also suggested me think about three things: electron excitation states, temperature, and beam energy, which all turned out to be critical factors in Atomic Engineering. It was not until the very final moment when I got recommendation letter from Ju for a postdoc position, that I knew all my advisors actually thought this topic was a risky choice.

It was indeed a risky choice if I was not struck by this last piece of luck. Nion, the electron microscope company, invited me to visit their campus after I expressed my willingness to have a summer internship there. During my visit, I met Wu Zhou, who authored multiple papers on single atom characterization and later became a professor back in China. He recommended me contact Prof. Juan-Carlos Idrobo, a staff scientist in Oak Ridge National Lab (ORNL) and a joint professor in University of Vanderbilt. To meet Juan in person, I attended the Microscopy and Microanalysis conference held in Columbus, Ohio. We discussed on the topic, I promised to submit a proposal to ORNL, and later, my proposal got accepted. The second problem was finally solved, and at the end of 2016, I embarked on this project.

The rest of my three years has been well depicted by this thesis, so no spoiler here.

I would like to acknowledge everyone above for being the most important guides on

my way to this thesis. Ju Li and Jing Kong, being my two advisors, gave me endless support and endorsement after I determined to commit to this project. I would also want to thank Juan-Carlos Idrobo for the time we spent together optimizing the microscope and for sharing his insights on the problem we encountered. Also, I want to thank Ondrej Krivanek and Niklas Dellby from Nion for giving me the opportunity to experience working in a boutique company that produce the world-class microscopes, to all my important collaborators, Toma Susi, Jani Kotakoski, Mingdong Dong, Zegao Wang, Zongyou Yin, Qing-Bo Yan for their contribution to this project. A special thanks to all the members from two groups, especially Cosmi Y. Lin, Haozhe Wang, Zhi Zhu, Kangpyo So, Yunfan Guo for the collaborations on the projects that yield a lot of fun.

Last but certainly not the least, I'm truly grateful to my parents who supported me along my way, and there no way I can express enough gratitude to my wife Zhuoxuan Li and my daughter Olivia for their steadfast encouragement and endless love in my hardest time.

Cong Su
Barker Library of MIT

Contents

1	The Renaissance of Atomic Engineering	17
1.1	Definition of atomic engineering	17
1.2	A history of single-atom manipulation	18
1.3	An introduction to aberration corrected STEM	20
1.4	Radiation damage as a good thing	21
1.5	Uncertainty in control process	22
1.6	Protecting 2D materials with a monolayer	22
1.7	The structure of this thesis	23
2	Single atom control using electron irradiation	25
2.1	Motivations of controlling single atoms from an application point-of-view	25
2.2	Electron-atom interaction	28
2.2.1	A simple two-body collision	28
2.2.2	Electron trajectory - orbital equation	31
2.3	Length and time scales	35
2.4	Dynamics of dopant atoms	38
2.5	Primary Knock-on Space	45
2.5.1	A detailed mathematical derivation of PKS	46
2.5.2	Doppler amplification effect	51
2.5.3	Manipulation decision tree	56
2.6	Discussion on Space Charge	60
2.7	The Influence of Excited States on Outcome Functions	62
2.8	Heat injection from electron beam	64

3	Corrosion inhibition of 2D materials with single-layer molecules	67
3.1	Motivations of corrosion inhibition	67
3.2	One-pot method for hexylamine deposition	68
3.3	Passivation Efficacy for Photodetectors	76
3.4	Broad Applicability of <i>n</i> -hexylamine Coating Method	77
3.5	Reversibility of <i>n</i> -hexylamine Coating	79
3.6	Final Thoughts	86
4	The Future of Atomic Engineering	87

List of Figures

2-1	Transferable energy from an electron to a carbon atom moving in the direction of the electron beam. The red and blue shaded areas mark the direct exchange and knock-out zones for a C neighbor to P. Inset: Schematic illustration of head-on collision between electron and C atom, with annotations matching the derivation above.	31
2-2	Scattering angle as a function of impact parameter. Inset: a blow-up of the curve close to impact parameter, $b=0$	34
2-3	The cross sections of different electron atom interaction processes. The atomic nucleus is represented by a purple circle in the middle, which is on the order of 10^{-15} m.	36
2-4	The time scale of five processes in the occurrence order: elastic collision, inelastic collision, excited state relaxation, lattice vibration relaxation, and electron interval time in STEM. “Step 1” indicates the “electron \rightarrow PKA” process, and “Step 2” indicates the “PKA \rightarrow lattice” process.	37
2-5	Illustration of competing experimental P dopant dynamics in graphene and its control.	39
2-6	STEM MAADF images (raw data) of the single-layer and double-layer graphene area where P dopant atoms are spotted.	41
2-7	Mechanisms of P dopant dynamics in graphene calculated with ab-initio molecular dynamics.	42
2-8	Comparison of dynamics of different impurity elements.	44
2-9	Primary Knock-on Space (PKS): a scheme for evaluating relative scattering cross sections of different dynamic processes.	47

2-10	The selective dynamics by tilting electron beam.	50
2-11	Derivation of final velocity of PKA when it is not static before interaction, by transitioning between lab frame and center of mass frame.	52
2-12	The modified ovoid when PKA is not static before interaction.	53
2-13	A decision tree for engineering atom configurations in doped graphene.	56
2-14	The selective dynamics from 55-77 structure back to honeycomb when beam tilted.	58
2-15	Elapsed time as a function of $\tilde{r} = r/r_0$ when $r_0 = 1 \text{ \AA}$. Left panel: when \tilde{r} is close to 1; right panel: when $\tilde{r} \gg 1$, which becomes a linear function.	62
3-1	Coating <i>n</i> -hexylamine on BP flakes and aging test with Raman spectroscopy.	69
3-2	The mechanism of <i>n</i> -hexylamine coating on BP.	72
3-3	Seven different configurations for direct adsorption of <i>n</i> -hexylamine on BP. For each configuration, the front view and side view are shown, and the adsorption energy is marked under each configuration. The largest adsorption energy is only 0.33 eV.	73
3-4	(A, C) For direct adsorption of <i>n</i> -hexylamine on BP, two special initial configurations have been tested, in which <i>n</i> -hexylamines are chemically bonded with BP. (B, D) After optimization, <i>n</i> -hexylamines in these two configurations have been repelled by BP, indicating that direct chemical bonding between <i>n</i> -hexylamines and BP is not possible.	74
3-5	Four different configurations for adsorption of <i>n</i> -hexylamine on oxidized BP. The largest adsorption energy is 0.419 eV, indicating that oxidization of BP can enhance adsorption between BP and <i>n</i> -hexylamine.	74
3-6	The binding energy of Various configurations when water molecule is involved.	75
3-7	The definition of coverage on BP.	75

3-8	The structures of HA-BP used for calculating H ₂ O and O ₂ molecules penetrating through the <i>n</i> -hexylamine coating. For each coverage and penetrating molecule type, three different locations are shown (far, middle, and close to the BP surface respectively), and each location is shown in two perspectives which are top view and side view. The distance <i>d</i> is defined in the first two figures of H ₂ O and O ₂ in 25% coverage.	81
3-9	Photodetectors and etching test.	82
3-10	Removability of <i>n</i> -hexylamine coating on BP by organic acid.	83
3-11	AFM data of the reversible process of <i>n</i> -hexylamine coating on BP and WSe ₂	84
4-1	The flow chart of one single step in Atomic Engineering with automatic image recognition and control feedback. The core of control strategy is determined by PKS theory developed in Chapter 3. Image credit: Nion.	88
4-2	The stacked structure of 2D materials. With the capability of penetrating through thin layers with little degradation of electron beam wave front, focused electron beams can be used for controlling atoms on different layers and harnessing the z-dimension.	89

List of Tables

2.1	Lifetime of inelastic excitations in some common 2D materials.	63
3.1	Coating parameters for amine and hexane molecules on 2D materials, for example BP in this work.	76
3.2	Coating parameters optimization of n-hexylamine on BP based on the protection testing results by taking optical microscope images before and after etching/oxidation of BP flakes. The etching method with H ₂ O ₂ (30% wt. in H ₂ O) etchant/oxidant follows: dip BP into H ₂ O ₂ for 20 sec, remove BP from H ₂ O ₂ , and leave dipped BP for 2 mins in air. Scale bars are 20 μ m.	78
3.3	Comparison between existing protection techniques. Factors such as coating layer thickness, resistive property, and techniques used are compared.	85

Chapter 1

The Renaissance of Atomic Engineering

1.1 Definition of atomic engineering

To begin with, we will discuss about the concept of “Atomic Engineering”, and its specific meaning related to this thesis. This terminology has been first used by Theodore von Kármán from California Institute of Technology in 1946, where he wrote [1]:

“And now it seems we are at the threshold of the new atomic age. I do not know whether or not this is true, but certainly, we shall have ‘atomic engineering’ in the fields of power and transportation. Are we prepared for the problems involved?”

The usage of “atomic” as a modifier in front of a noun is usually interchangeably used with “nuclear”, where cases of “atomic bomb” or “atomic power” follow. However, the usage of “nuclear bomb” or “nuclear power” are more proper here, as in these cases, it is only nucleus being a part of atom that plays the critical role, while the electrons outside of nucleus plays a minimum role. When “atomic” is used as an adjective, it should refer to an entity or event involving the *whole* atom. “Engineering”, on the other hand, is defined in Wikipedia as “the use of scientific principles to design and build machines, structures, and other items”. The human interactions

with the surrounding nature can be categorized by the direction of information flow as: learning from the environment (human input), and modifying the environment (human output). It happens likewise as how we distinguish the knowledge body into “science” and “engineering”. “Science” falls into the first category, where human gets input from the outside world and process this set of information with induction and conduction. “Engineering” belongs to the latter category, where human utilize the knowledge pool established from “scientific learning” and make an output back to the nature to modify something. Therefore, “Atomic Engineering” might be a superset of nuclear engineering, where it can be defined as “exploiting the atomic characters of matter for engineering applications”. From this definition, atomic engineering refers to any engineering purpose that harnesses the different degrees of freedom of an atom, such as its spatial location and the electronic state. In our thesis, we focus only on the atom location, as the definition is further narrowed down to “controlling the atomic configuration of matter for engineering applications”. This definition has confined our event to be mainly within the realm of “controlling the position of atoms” or “atom-by-atom fabrication” for realizing an application that might be only reachable by controlling the structure down to atomic scale.

1.2 A history of single-atom manipulation

To zoom out our scope a bit, ultra-fine machinery in engineering has always been dubbed as a critical technique in high-end manufacturing. Traditionally, the materials are created using a “top-down” method, where the synthesis process itself is the focus of the materials fabrication and the target material is created as-a-whole. Macroscopic parameters such as temperature, pressure, chemical precursors, gas environment, electric voltage, magnetic field etc., are tuned for reaching the final product that is also desired and expected to manifest a homogeneous property in a long range scale. By switching these external parameters, it is possible to modulate the frontier boundary of the material during growth process (the 0D frontier end of a 1D material, the 1D frontier edge of a 2D material, or the 2D frontier surface of a 3D material), but

it is impossible to control the features of a materials that is two-dimension lower (like controlling a 0D defect feature in 2D materials). A more advanced structural control technique renders more capability in quality control and more flexibility in materials design process. The ability to create structures with special units in a short-range scale (in our case, as short as the length scale of an atom) could integrate various functions condensed in a small footprint, with the feature density of n^2 compared with n as in tuning the macroscopic parameters. This “bottom-up” view of creating material structures is reminiscent of transistors and integrated circuit devices flourished in the 20th century, where transistors with different functional units are integrated into a single chip board, following a trend predicted by the renowned Moore’s Law [2]. With unit transistors reaching the size of several atomic scale, the developing trend of the transistor industry no longer follows Moore’s Law, where traditional fabrication method fails as expected and quantum effect turns to dominate at this length scale [3]. Investigating the atomic scale properties (where localization effect dominates and the periodic boundary condition in a crystal-viewpoint no longer holds) and looking for a path to control single atoms (where each atom needs to form a certain structure as designed) are essential and urgently needed. Thus, controlling single atom can be regarded as an ultimate form of material engineering where the smallest unit that still represent the property of the substance act as a building block. By scaling up the control steps, a group of engineered atoms collectively contributing to a pre-designed function. With one order of magnitude lower in scale than nano-engineering (10^{-9} m), atomic engineering (10^{-10} m) is deemed to be much more difficult. Almost two decades ago, scanning tunneling microscope (STM) demonstrated its first success in manipulating adsorbed atoms on the metal surface [4, 5]. It is followed by atomic force microscope (AFM) which also showed its capability in moving vacancies on the surface [6]. Due to the complexity of designing the atomic-scale AFM when compared with STM, it is not until about 19 years after its invention has the AFM successfully manipulated the first atom. STM and AFM belong to a superset category called scanning probe microscope (SPM). The problems of controlling atoms using SPMs are evident:

1. Low temperature: The samples are usually kept under very low temperature, which usually needs liquid helium to stabilize.
2. Slow: The mechanical movement of metal probe is very slow.
3. Surface limitation: Only the atoms on the surface of bulk material can be modified.

How to address these problems is critical in up-scaling Atomic Engineering which is the main point of this thesis.

1.3 An introduction to aberration corrected STEM

Other than SPMs, another imaging technique that has atomic resolving capability is scanning transmission electron microscope (STEM) has a much longer history than the above SPMs, but it was not until the success invention of aberration-corrector that the true atomic resolution images can be routinely obtained by normal users. “Aberration” of an optical component (or electron optical component in our context) is a deviation from the ideal light path that is intended to be created, mainly caused by intrinsic physical law or the defective manufacturing of an optical component. For example, in a traditional electron microscope, the electrons are focused by the round electromagnetic lens which creates an electromagnetic field. In 1936, Scherzer proved that no matter how these round lenses are modified, they all suffer from a 3rd-order spherical and first-order chromatic aberration [7]. The consequence of having such an aberration is that the electron probe cannot be focused onto the same length scale as a single atom. Later, he proposed that by using multipole magnetic lenses, these aberrations can be compensated, which leads to the invention of modern corrector. With the aberration fixed by the corrector, the width of electron probe is improved to be 1 \AA , on the order of the size of an atom. The capability of focusing high energy electrons on an atom directly leads to the advent of atomic-resolved imaging and single-atom spectroscopy [8,9]. This also creates opportunity to selectively focus electron beams to modify a single atom.

1.4 Radiation damage as a good thing

Due to the nature of electron beam, it is only the projection image along the z-direction of the materials that can be created (except for confocal techniques which still has a z-direction resolution on the order of 10 nm). With the layer distance to be around half a nanometer, no atomic-level information can be extracted layer-by-layer inside STEM/TEM; therefore, it is only an “atomic column” that can be put under electron beam and no atom manipulation can be done. The birth of two-dimensional (2D) materials have changed this situation. With only one-atomic layer, WYSIWYG (“what you see is what you get”) is truly realized in STEM. The atom species can be distinguished by the contrast of atoms (Z-contrast imaging [10]) or the single-atom electron energy loss spectroscopy (EELS) [11].

STEM has been designed as a tool for “seeing” atoms in the first place. The radiation damage from high energy electron beam on materials has always been a side effect that is to be avoided rather than embraced in STEM. It was not until decades later it was invented, the true demonstration of successful single-atom manipulation was done by Susi etc. [12] and Dyck etc. [13]. It is at this time point that the radiation damage is truly turned from something bad to good.

When comparing these atom-control techniques, they should be categorized into two different groups, according to the energy barrier involved in moving the atoms: (1) STM and AFM control the surface adsorbed atoms which lightly adhere to the surface of host matrix through van der Waals interaction, and the metal uses what is called “metallic adhesion” to push or pull the atom [14]. Like 3D printing, STM and AFM can in principle pile up a structure atom-by-atom thanks to the nature of surface modification. The built-up atomic pile is the functional structure with rather small coupling to the substrate. (2) On the contrary, STEM modifies the crystal structure and covalent chemical bond. The atom manipulation involves a bond breaking on the energy level of 10 eV and a reformation of chemical bonds afterwards. This modification can only be realized by high energy electrons (30-200 keV) which is able to transfer enough energy to atoms (~ 10 eV for low Z elements) for completing this

task. Since the atom is covalent-bonded to the materials structure, local density of states (DOS) of the host matrix will be altered through the modification of atom position, which may be coupled to other properties of the host matrix.

1.5 Uncertainty in control process

In this thesis, we use STEM to both drive and identify the atomic motion of individual phosphorus (P) dopants in graphene, and construct a theoretical scheme for evaluating their relative probabilities with respect to electron energy and momentum direction [15]. In stark contrast to the Si dopant where the movement is relatively easy to induce, P is much harder to control. When we try to move P atom, what we found is that various dynamics process is induced instead of the dynamic we desire. These dynamic processes are categorized into four types: (A) direct exchange and (B) Stone-Wales (SW) transition, which conserve the atoms, plus (C) knockout of a carbon neighbor and (D) replacement of a dopant atom by C, which do not conserve the local composition. We choose to use 60 keV electron energy (electron velocity is $0.4462c = 1.3377 \times 10^8$ m/s) to minimize (C)+(D) while maximizing the rates of direct exchange and SW transition. Just like the Si case, instead of aiming the electron beam directly at the dopant itself, it has been established that dynamics can be more effectively induced when the electron beam is aimed at a carbon neighbor of the dopant [12, 16]. Our goal in this thesis is to maximize the desire probability while reducing the undesired ones.

1.6 Protecting 2D materials with a monolayer

Other than graphene and hexagonal boron nitride (hBN), almost all the other 2D materials are easy to get corroded in air [17]. One biggest problem during the materials transport between MIT and ORNL is that some of the samples degrade very fast, and we cannot preserve its original crystal lattice after a long flight. That motivates me to investigate further into this, where our goal is to preserve the crystal lattice

of 2D materials as intact as possible during transport, and when we arrive at the destination, the protection layer is still able to be removed.

But this is by no means an easy task. When we consider kinetic passivation of two-dimensional (2D) crystals [18–23], it should be even more essential because (a) the thickness of passivation layer $d_p(t)$ on 3D materials like Si, Al, Mg etc. stays 3-5 nm over very long time t , which is insignificant fraction of the remaining unreacted material. However, one cannot say this for a thin 2D material whose total thickness is d_s , which is likely comparable to $d_p(t)$. In other words, we must ensure $d_s > 2d_p(t)$ for a free-standing sample over an extended period in order to utilize the intrinsic properties of the native material exposed to ambient environments. (b) The functional properties of 2D crystals are extremely sensitive to its thickness (i.e. $d_s - 2d_p(t)$) down to a single monolayer. Therefore, meticulous corrosion control down to the level of few-/single-layer is practically useful. (c) The thickness and type of passivation might also provide a natural opportunity to engineer extremely thin vertical heterostructures for information processing applications. For these reasons, fundamental study of passivating 2D crystals is important, in addition to its obvious practical significance.

1.7 The structure of this thesis

This thesis consists of two main sections. Chapter 2 is going to introduce the background of elastic and inelastic atom-electron interacts, and the typical length scales and time scales of various dynamic processes. Then we will get into the dynamics of single atomic dopant under the irradiation of high energy electron source. A theoretical framework called Primary Knock-on Space (PKS) will be developed for optimizing the atom control process. Several caveats of electron-atom interaction is also discussed with detailed derivations. Chapter 3 deals with the corrosion problem of 2D materials, where a molecular monolayer is deposited on the protected 2D materials. To start with, the coating procedure and parameters are carefully chosen, and detailed characterizations have done to investigate the structures of the thin coating. Application-wise, a photoelectric device with the coating has been demonstrated to

be effective in resist harsh environment. A density function theory (DFT) model is used to interpret the mechanism and shows the waterproof function of the surface layer. Finally, Chapter 4 serves as an envision of the possible applications of PKS in Atomic Engineering, and where Atomic Engineering might leads to. We propose an architecture where controlling atoms is done with automatic program controlled by PKS theory. We also propose at the end a 3D stacking architecture harnessing the penetration depth of high energy electrons.

Chapter 2

Single atom control using electron irradiation

2.1 Motivations of controlling single atoms from an application point-of-view

As nanotechnology has been developed into a well-integrated realm consists of science, engineering, and technology that manipulates matter from 1nm to 100nm, we have hit some limits that is bounded by the physical law "on the bottom". The state-of-the-art nanotechnology might push this limit down to 1 nm by integrating carbon nanotubes into transistors. That seems to be a small enough transistor size, until we realize that shrinking size by one order of magnitude in transistor may only takes about 5-10 years before. The scale level that goes beneath the nanometer-level is the atomic level, and surface atom manipulation has only been done by STM three decades ago. The limitation of surface scanning as well as the stringent operation conditions of STM also confines its application and its transition to the real world. Here, we are designing another way of manipulating the atoms from the ground-up using electron microscope.

Atomic Engineering is defined in the introduction as "controlling the atomic configurations of matter for engineering applications". Apart from STM, most of the

other control in sub-atomic level is fulfilled by manipulating nuclear spin, while keeping the atom configuration untouched, as in nuclear magnetic resonance (NMR). In NMR, the configuration of atoms are kept intact, while only the nuclear spin is controlled by the external field. However, the motivation to modify materials on atomic level is quite strong and self-evident. On one hand, it is human instinct that we should proactively seeking fabrication tools that renders us with more precision. On the other hand, cranking up areal density for memory is a tendency driven either by the business market or an idiosyncrasy of following the Moore's Law [24], which rules the semiconductor world for decades and hardly failed. Assuming if Moore's Law still works for the next several decades, we need to be able to control single atoms for storing information in 25 years.

Given the fact that Atomic Engineering might be applied in information storage, it is warranted to have a very brief introduction of storage technology history here and how Moore's Law can fail. Information storage technology is developing rapidly thanks to the much more sophisticated manufacturing process in nano-materials and a deeper understanding in optical and magnetic physics. In 2007, Albert Fert and Peter Grunberg were awarded the Nobel Prize in Physics for the discovery of giant magnetoresistance (GMR), paving the foundation of the present hard disk drive industry. In the mid-2000s, when the magnetized recording domain becomes smaller, people started to realize that the so-called superparamagnetism is a pressing issue [25]. In large uniaxial anisotropy material, spontaneous reversal of the magnetization vector could happen when the temperature is high enough. Grain magnetization flipping is a thermal activation process governed by the Néel-Arrhenius equation giving a time constant τ :

$$\frac{1}{\tau} = f_0 \exp(-E_B/k_B T) \quad (2.1)$$

where f_0 is the attempt frequency determined by intrinsic magnetic properties and is of the order of $10^9 - 10^{12}$ Hz, and E_B is the energy barrier between the transition

of two states of the magnetic polarization of a grain, which could be calculated as $E_B = K_u V$ where K_u is the uniaxial constant of a material, and V is the grain volume. The key issue needs to resolve in a traditional hard disk drive industry are reconciling a trilemma involving grain size, media anisotropy, and the write element magnetic field [25]. Grain size and media anisotropy are two “conjugate” quantities which is hard to be improved together, which could be seen in Equation (2.1): when the grain volume shrinks down, the activation barrier becomes smaller, and the vector flipping becomes more frequent. A large write element magnetic field is required to flip the magnetic polarization, which is usually 2.4 Tesla by using CoFe head developed early in 1990s, and no more increase thereafter [25]. These three quantities together define the performance of the data recording media, and an upper ceiling is about to be hit. If we want to continue the trend of transistor development, new ways to control atoms needs to be found in order for the device to work properly in room temperature.

To reiterate, controlling the exact atomic structure of materials is an ultimate form of engineering [26, 27]. Atomic manipulation and atom-by-atom assembly can create functional structures that are hard to synthesize chemically [16, 28–30], e.g. positioning atomic dopants exactly to modify the properties of carbon nanotubes and graphene [31]. Nitrogen (N) or phosphorus (P) dopants might be useful in quantum informatics due to non-zero nuclear spin [32], similar to the use of the nitrogen vacancy (NV) center.

Successful atomic engineering requires understanding of two parts:

1. how the desirable local configurational changes can be induced to increase the speed and success rate of control;
2. how to scale up basic unit-processes into feasible structural assemblies of 1-1000 atoms to produce the desired functionality.

Historically, scanning tunneling microscopy (STM) [33] have demonstrated good stepwise control of single atoms, leading to physicochemical insights and technological advances [34]. However, their scalability and throughput are severely limited by the mechanical probe movements. Scanning transmission electron microscope (STEM)

is an optical-microscope-equivalent using electron source for imaging. With the development of aberration corrector, it can focus electron beams into fine probes with a full width half maximum at around 1 Å. It has emerged as a versatile tool for characterizing the precise atomic structure of materials [8, 9, 35–41]. Despite its very early stage of development, STEM also shows great promise as a tool for atomic manipulation: in two-dimensional (2D) graphene, Si dopants are found to be stepwise controllable [13, 41, 42] and iterating these basic steps enables long-range movement with a high throughput [43], whereas in a three-dimensional (3D) silicon crystal, the projected location of Bi dopants was also manipulated [44]. However, imprecise understanding of the dynamics of the basic steps, which involves relativistic electron-nucleus collisions, electronic excitation and relaxation, dynamic ion trajectories, momenta dephasing and heat conduction, add uncertainty to this technique. While the traditional theory of radiation damage provides a basis for understanding, instead of trying to minimize beam effects atomic engineering seeks to control them in order to achieve desired configurational changes. Concepts like the displacement threshold energy E_d , which is in most cases approximated as scalar, turns out to be too crude to guide the design of the precise branching rates of different configurational outcomes [45, 46].

2.2 Electron-atom interaction

2.2.1 A simple two-body collision

The transferrable energy from a high energy electron to a static carbon atom can be estimated using the following relation:

$$E = \frac{\tilde{E}_e(\tilde{E}_e + 1.02)}{496A} \sin^2 \frac{\psi}{2} \quad (2.2)$$

where \tilde{E}_e is the incident electron energy in MeV, E is the transferred energy to a static nucleus in MeV, A is atomic mass number (e.g. ~ 12 for carbon), and ψ is the scattering angle of the electron (when $\psi = 0$ no interaction happens and $E = 0$; when $\psi = \pi$, back scattering happens and E is maximum). It can thus be estimated that

the maximum energy transferable to a C atom is 10.9 eV for a 60 keV electron, which would mean that all dynamic processes should be prohibited since the lowest energy required for inducing a lattice change in P-doped graphene is larger than 14 eV.

However, the lattice of graphene is not static. Due to thermal vibrations, the atoms of the lattice are in motion, which relaxes the momentum conservation condition and increases the transferable energy under the irradiation of a high energy electron beam. Even at 0K, the zero-point energy resulted from Heisenberg uncertainty principle would also leads to a non-static atom dynamics. The contribution from this lattice vibration will be discussed in detail in the following Doppler Amplification Effect section. Here, to simplify the picture, our following derivation assumes a head-on collision between an electron and a C atom ($\theta_e = 0$).

Consider the conservation of momentum and energy, we have

$$\tilde{\mathbf{p}}_e + \tilde{\mathbf{p}} = \mathbf{p}_e - \mathbf{p}, \quad (2.3)$$

$$\tilde{E}_e + \tilde{E} = E_e + E, \quad (2.4)$$

where $\tilde{\mathbf{p}}_e$, \tilde{E}_e , \mathbf{p}_e , E_e denote the momentum and energy of electron before (with \sim) and after (without \sim) collision, with $\tilde{\mathbf{p}}$, \tilde{E} , \mathbf{p} , E being the counterparts for the nucleus. The momentum is related to energy relativistically for the electron (inside STEM, the electron is traveling at half of the light speed), and non-relativistically for the nucleus:

$$|\mathbf{p}_e| = \frac{1}{c} \sqrt{2E_e E_0 + E_e^2}, \quad (2.5)$$

$$|\mathbf{p}| = \sqrt{2ME}, \quad (2.6)$$

and the pre-collision also follows the same form of the above equations. We therefore

get

$$\frac{1}{c}\sqrt{2\tilde{E}_e E_0 + \tilde{E}_e^2} + \sqrt{2M\tilde{E}} = \sqrt{2ME} - \frac{1}{c}\sqrt{2(\tilde{E}_e + \tilde{E} - E)E_0 + (\tilde{E}_e + \tilde{E} - E)^2}. \quad (2.7)$$

Since the kinetic energy of the nucleus is much smaller than that of the electron in all stages, we can approximate $\tilde{E}_e + \tilde{E} - E$ into \tilde{E}_e , and get the following expression:

$$\sqrt{2ME} = \sqrt{2M\tilde{E}} + \frac{2}{c}\sqrt{2\tilde{E}_e E_0 + \tilde{E}_e^2}. \quad (2.8)$$

For a static nucleus before collision ($\tilde{E} = 0$), we have

$$\sqrt{2ME_{\text{stat}}} = \frac{2}{c}\sqrt{2\tilde{E}_e E_0 + \tilde{E}_e^2}, \quad (2.9)$$

where E_{stat} is the transferred energy from electron to a static atom. Subtracting the above equations gives

$$\sqrt{E} = \sqrt{\tilde{E}} + \sqrt{E_{\text{stat}}}. \quad (2.10)$$

This relation between the final energy of PKA (E) and the atom vibration energy (\tilde{E}) can be plotted as Figure 2-1. Therefore, to activate a direct exchange process, a vibration energy of 0.5 eV is enough. Although the average kinetic energy of atoms at room temperature is much smaller (0.025 eV), their velocities follow a normal distribution with a width given by the mean-square velocity (or corresponding kinetic energy), leading to a finite population of atoms with high kinetic energies at the moment of impact.

The probability distribution of out-of-plane velocities of carbon atoms in graphene can be estimated using [47]:

$$P(v_z, T) = \frac{1}{\sqrt{2\pi v_z^2(T)}} \exp\left(-\frac{v_z^2}{2v_z^2(T)}\right) \quad (2.11)$$

To get a sense of how rare these events are, the probabilities of vibrational energy above a certain level are: (1) 0.1 eV: 0.0122; (2) 0.2 eV: 7.2×10^{-4} ; (3) 0.3 eV: 4.8×10^{-5} ; (4) 0.4 eV: 3.3×10^{-6} ; (5) 0.5 eV: 2.4×10^{-7} . Although large kinetic energies are

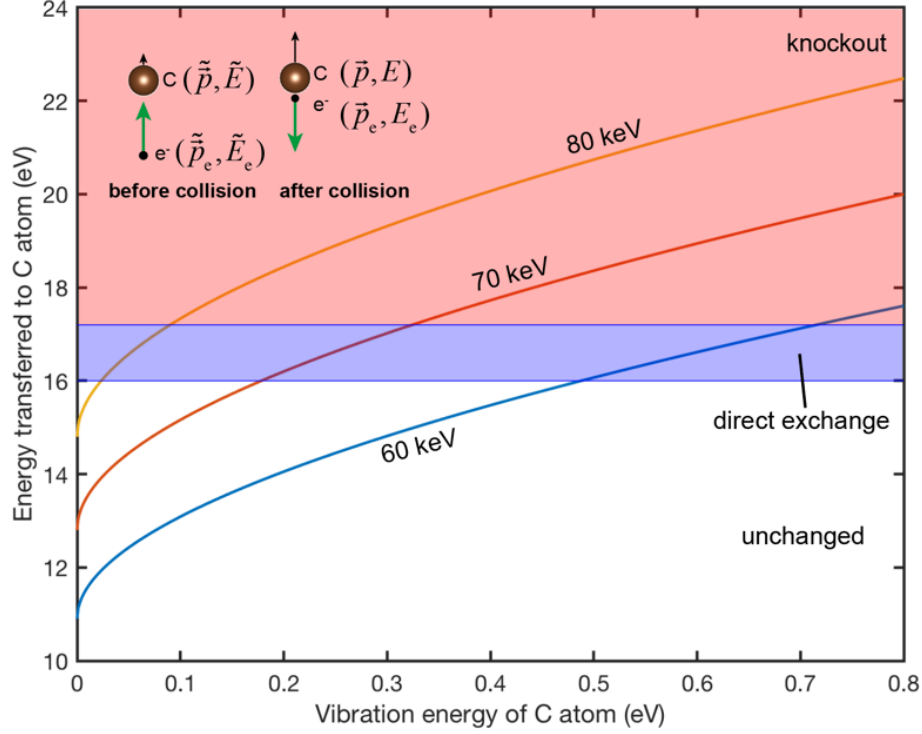


Figure 2-1: Transferable energy from an electron to a carbon atom moving in the direction of the electron beam. The red and blue shaded areas mark the direct exchange and knock-out zones for a C neighbor to P. Inset: Schematic illustration of head-on collision between electron and C atom, with annotations matching the derivation above.

rare, such vibrations do yield finite cross sections for events that would be otherwise forbidden.

2.2.2 Electron trajectory - orbital equation

Most of the time, electron does not hit right onto the nucleus and make back scattering. Therefore, the trajectory of the electron is critical when the impact parameter of electron, b , is larger than 0. Here, we introduced a very important variable “impact parameter” which is defined as the perpendicular distance between the path of a projectile and the center of a potential field created by an object that the projectile is approaching. In a two body system, the total energy is conserved

$$E = \frac{1}{2}\mu(\dot{r}^2 + r^2\dot{\theta}^2) + U(r) \quad (2.12)$$

and the total angular momentum is conserved

$$l = \mu r^2 \dot{\theta} \Rightarrow \dot{\theta} = \frac{l}{\mu r^2} \quad (2.13)$$

where $U(r)$ is the potential between the two bodies, and μ is the reduced mass for the two bodies. l is the angular momentum, θ and r are the angle and distance with respect to origin in the polar coordinate. The dot above the variables represent time derivative, d/dt . Getting rid of $\dot{\theta}$ by combining the above two equations, and by approximating μ to be m as $M \gg m$,

$$E = \frac{1}{2} m \dot{r}^2 + \frac{l^2}{2mr^2} + U(r) \quad (2.14)$$

and solving for \dot{r} , we have

$$\dot{r} = \pm \sqrt{\frac{2}{m} \left(E - \frac{l^2}{2mr^2} - U(r) \right)}. \quad (2.15)$$

For orbital equation, we are interested in $dr/d\theta$, so by using chain rule,

$$\frac{dr}{d\theta} = \frac{\dot{r}}{\dot{\theta}} = \pm \sqrt{\frac{2m}{l^2}} r^2 \sqrt{E - \frac{l^2}{2mr^2} - U(r)}. \quad (2.16)$$

therefore,

$$\theta = \int d\theta = \pm \frac{l}{\sqrt{2m}} \int dr \frac{1}{r^2 \sqrt{E - \frac{l^2}{2mr^2} - U(r)}}. \quad (2.17)$$

Specifically, in our system, $U(r) = -\frac{kQq}{r}$, so we have

$$\theta = \pm \frac{l}{\sqrt{2m}} \int dr \frac{1}{r \sqrt{Er^2 - \frac{l^2}{2m} + kQqr}}. \quad (2.18)$$

Using

$$\int \frac{dr/r}{\sqrt{a + br + cr^2}} = \frac{1}{\sqrt{-a}} \sin^{-1} \left(\frac{br + 2a}{r\sqrt{b^2 - 4ac}} \right) \quad (2.19)$$

we get

$$\theta - \theta_0 = \pm \sin^{-1}\left(\frac{kQqr - l^2/m}{r\sqrt{k^2Q^2q^2 + 2l^2E/m}}\right) \quad (2.20)$$

which is equivalent to

$$r = \frac{l^2/kQqm}{1 \pm \epsilon \sin(\theta - \theta_0)} \quad (2.21)$$

where

$$\epsilon = \sqrt{1 + \frac{2l^2E}{k^2Q^2q^2m}}. \quad (2.22)$$

By convention, we choose "+" sign and $\theta_0 = \frac{\pi}{2}$,

$$r = \frac{l^2/kQqm}{1 + \epsilon \cos \theta} \quad (2.23)$$

By converting angular momentum $l = mvb$ where b is the impact parameter of electron with respect to the hitting target atom, and $E = 60$ keV,

$$\epsilon = \sqrt{1 + \frac{2mv^2b^2E}{k^2Q^2q^2}}. \quad (2.24)$$

One very useful application of equation (2.23) is that we can calculate the scattering angle of electron at a given impact parameter, b . The incoming angle of electron, θ_0 , can be calculated by setting

$$1 + \epsilon \cos \theta_0 = 0. \quad (2.25)$$

For example, with an impact parameter of $b = 1 \times 10^{-13}$ m, we have $\epsilon = 1.187$, and $\theta_0 = 147.4^\circ$. Therefore, the deflected angle is $\alpha = 2\theta_0 - 180^\circ = 114.8^\circ$. The corresponding PKA scattering angle is 32.6° . A relation between the scattering angle and impact parameter is shown in Figure 2-2.

The electron trajectory is important to know since the energy transferable from an electron to an atom depends on the out-scattering angle of the electron. Dynamics can only happen when the scattering angle is large enough such that there are enough energy transferred from electron to the target atom. By using the trajectory equation,

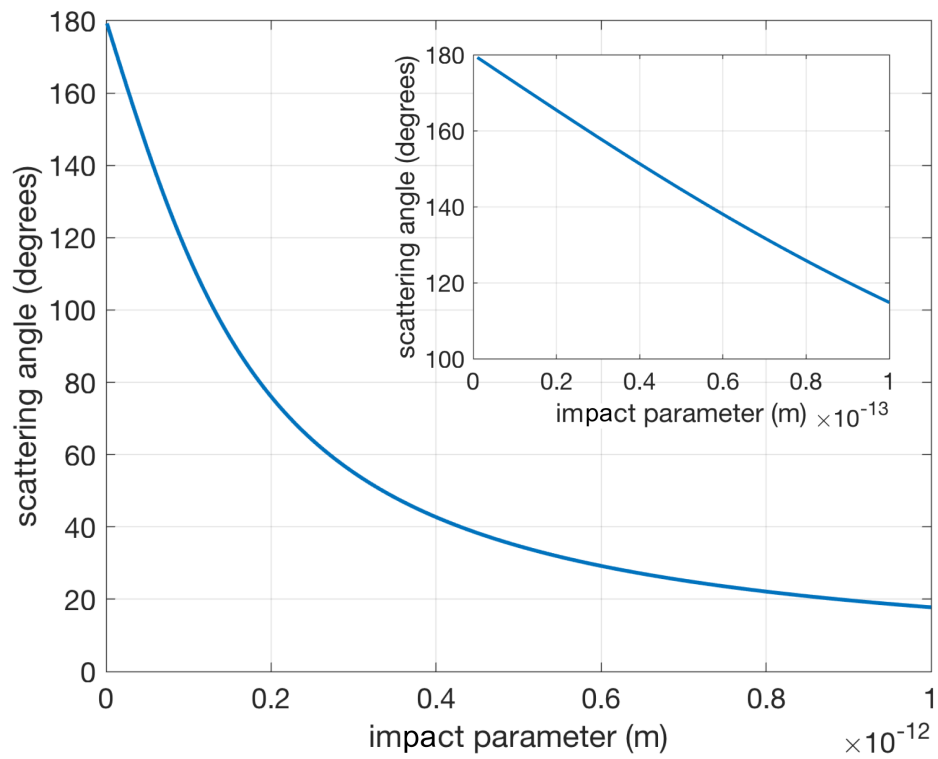


Figure 2-2: Scattering angle as a function of impact parameter. Inset: a blow-up of the curve close to impact parameter, $b=0$.

we can therefore estimate the cross section of a certain dynamics very easily by knowing the minimum scattering angle required.

2.3 Length and time scales

If we stand from the electron standpoint of view, and looking down on the target atoms, what we see looks like the Figure 2-3. The figure is drawn in logarithm scale for clarity, so if we convert the scale to linear scale, what one can imagine is that the area (or what is called “cross section” here) is very small for the region of where dynamics can be induced. To estimate the effective number of electrons that can induce a dynamic process, we assume 10^9 electrons/s (160 pA) as the current inside STEM. The FWHM of electron probe is proved to be around 1\AA so there is only 10^{-8} of the total electrons can be used for inducing the dynamics. That is, for every second, there are only 10 electrons inside the microscope that fly into the cross section that can truly induce the dynamics (let’s call them “effective electrons”). In our experiment, we sometimes see that dynamics happens very fast, causing some broken rows in the scanning image.

To achieve atomic configurational change, the post electron collisional energy of the primary knock-on atom (PKA; here it is carbon), E , needs to be on the order of 10 eV. This requires the penetrating electron to pass very close to the PKA nucleus (impact parameter $b < b_c \sim 10^{-14}$ m), with corresponding collisional cross-section on the order of barns ($\sigma \sim 10^{-28}$ m²) (please refer to Figure 2-4). Such elastic collision and large energy transfer occur mainly within zeptosecond timescale ($\tau_c \sim 10^{-22}$ s), inducing a post-collisional PKA momentum labelled by a vector. With a total beam current of $I \sim 50$ pA, this amounts to about 1 relativistic electron penetrating the graphene every 3 nanoseconds ($\tau_p \equiv e/I \sim 3$ ns), and one can focus the e-beam to a spot with a full-width at half-maximum (FWHM) of 1\AA (which provides a sufficient description of the scanning beam). The collisional probability (defined as imparting the PKA with $E \sim 10$ eV energy, that may cause “immediate” configurational change within picoseconds) is thus only $\sim \sigma/\text{FWHM}^2 \sim 10^{-8}$ per penetration event,

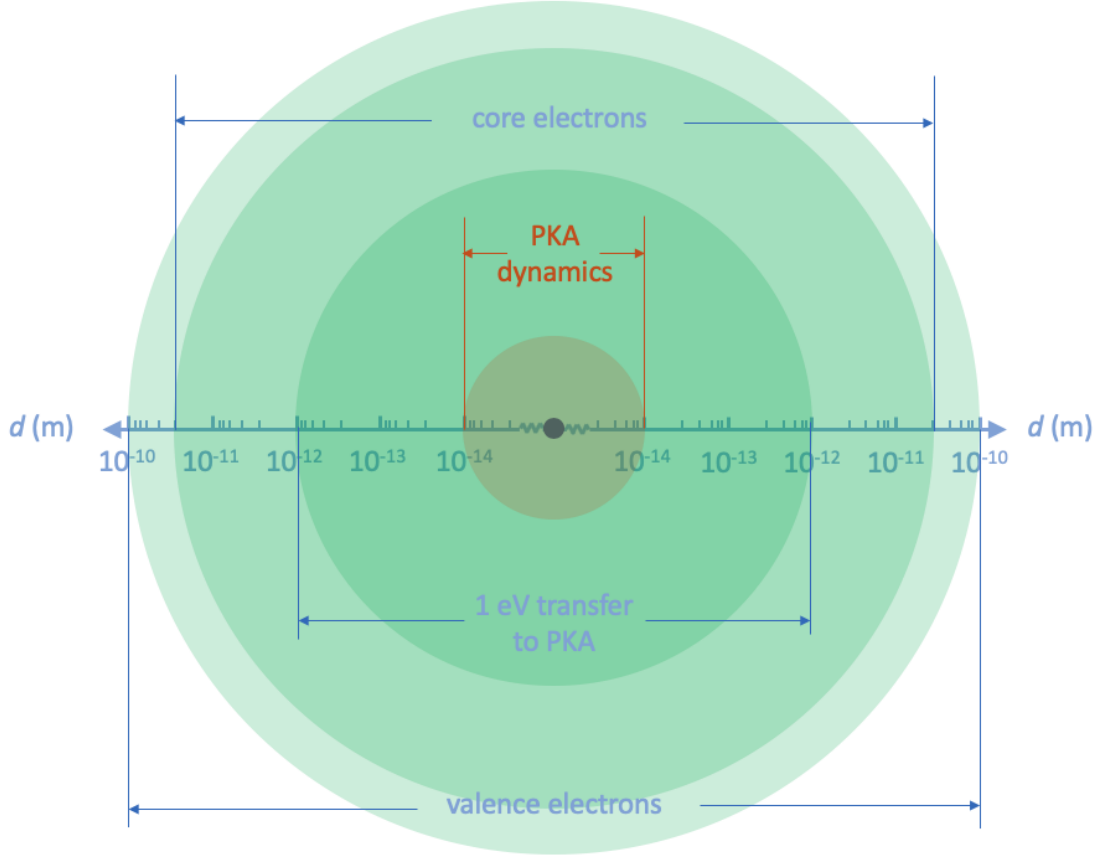


Figure 2-3: The cross sections of different electron atom interaction processes. The atomic nucleus is represented by a purple circle in the middle, which is on the order of 10^{-15} m.

or $\sigma/\text{FWHM}^2/\tau_p \sim 10$ per second (0.1 per second for events like direct exchange with cross section of 0.01 barn); the rest of the penetration events cause electronic excitation and small ionic rattling, but not immediate local configurational change.

Regardless of whether a penetrating electron gets within b_c or not, a penetration event will cause electronic excitation, occurring with attosecond timescale $\tau_e \sim 3.4 \text{ \AA}/\tilde{v}_e \sim 10^{-18}$ s (3.4 \AA being the graphene thickness), which however in the case of graphene will relax collectively on the femtosecond timescale ($\tau_E \sim 10^{-15}$ s) to the electronic ground state [48]. Thus after $\tau_e + \tau_E$, the electronic subsystem falls back to electronic equilibrium and one may use the Born-Oppenheimer (BO) approximation to describe the ion dynamics, that can either achieve the (A)-(D) configurational change (labelled by $i=1\dots 4$) or unchanged ($i=0$) on the BO surface, within a few

picoseconds ($\tau_I \sim 10^{-12}$ s). Since $\tau_I \gg \tau_e + \tau_E$, it is justified here to apply ground-state density functional theory (DFT) to track the main portion of the ion dynamics, to obtain the probability of success, P_i , of dynamics that lead to configurational outcome i . Throughout $t = \tau_c, \tau_E, \tau_I$, the PKA momentum history needs to be tracked, thus we build a theoretical scheme called Primary Knock-on Space (PKS) for estimating the relative scattering cross sections of different electron-induced dynamics due to either sample or electron beam tilt, and for selectively activating the desired outcomes. We further provide experimental verification of our calculations, thus opening new avenues for atomic engineering using focused electron irradiation.

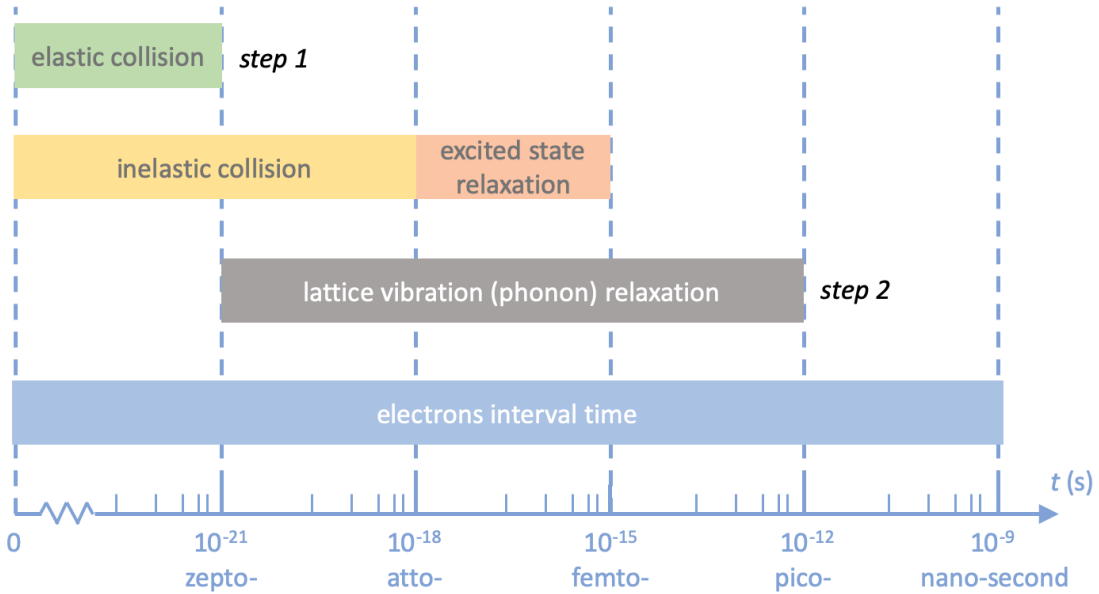


Figure 2-4: The time scale of five processes in the occurrence order: elastic collision, inelastic collision, excited state relaxation, lattice vibration relaxation, and electron interval time in STEM. “Step 1” indicates the “electron \rightarrow PKA” process, and “Step 2” indicates the “PKA \rightarrow lattice” process.

We find that the P dopant in graphene can serve as a good example for covering many categories of electron-induced dynamics. With highly collimated and focused (e-beam FWHM 1 \AA) electron irradiation on a carbon atom neighboring the phosphorus dopant, we occasionally create a single energetic PKA, with rate $\sim d\sigma/\text{FWHM}^2/\tau_p$, where $d\sigma$ is the differential cross-section corresponding to a particular post-collisional PKA differential momenta volume. To clarify, the term PKA exclusively refers here to

the energetic carbon neighbor of the phosphorus dopant, so "PKA" and "C neighbor colliding with an electron of the beam" are equivalent throughout this paper. This energetic carbon atom then drives a short burst of atomic motions nearby within $\tau_1 \sim$ picoseconds.

2.4 Dynamics of dopant atoms

In Figure 2-5, four types of dynamics are shown, categorized into two groups: atom-conserving dynamics (which is desirable) and atom-non-conserving dynamics (which is often not desirable). Atom-conserving dynamics include (A) direct exchange between P and C [Figure 2-5(A), earlier dubbed "bond inversion" in the context of Si [12]], and (B) SW transition [Figure 2-5(B)], i.e. 90° rotation of a P-C bond [46]. Atom-non-conserving dynamics include (C) knockout [Figure 2-5(C)] where the PKA is knocked out by the electron beam (P turns from three-coordinated to four-coordinated, after which we found it is no longer possible to further manipulate the configuration with 60 keV e-beam), and (D) replacement [Figure 2-5(D)], where a diffusing carbon adatom that happens to be nearby receives energy from a penetrating electron and replaces the dopant. Such wandering C adatoms are always present on graphene surfaces [12, 49], but they diffuse too quickly to be imaged. In the above experiments, we scanned the beam over a square area covering the dopant atom so that the configurational changes could also be captured in frames (often as a broken "transit" frame, where part of the scanned image is discontinuous with the rest of the image that is scanned later).

In Figure 2-5(A), three consecutive frames of direct exchange including a transition frame are presented. As a result, the P dopant atom exchanges site with the PKA while the e-beam is scanning from left to right across the PKA (white dashed line; note that at each pixel, most of the electron dose is distributed within an \AA -sized area surrounding it according to the beam intensity profile). In Figure 2-5(B), a SW transition is preceded by a direct exchange. After the direct exchange (frame 1 to 2), the P-C bond is rotated by 90° (frame 2 to 3), and the hexagonal lattice is locally

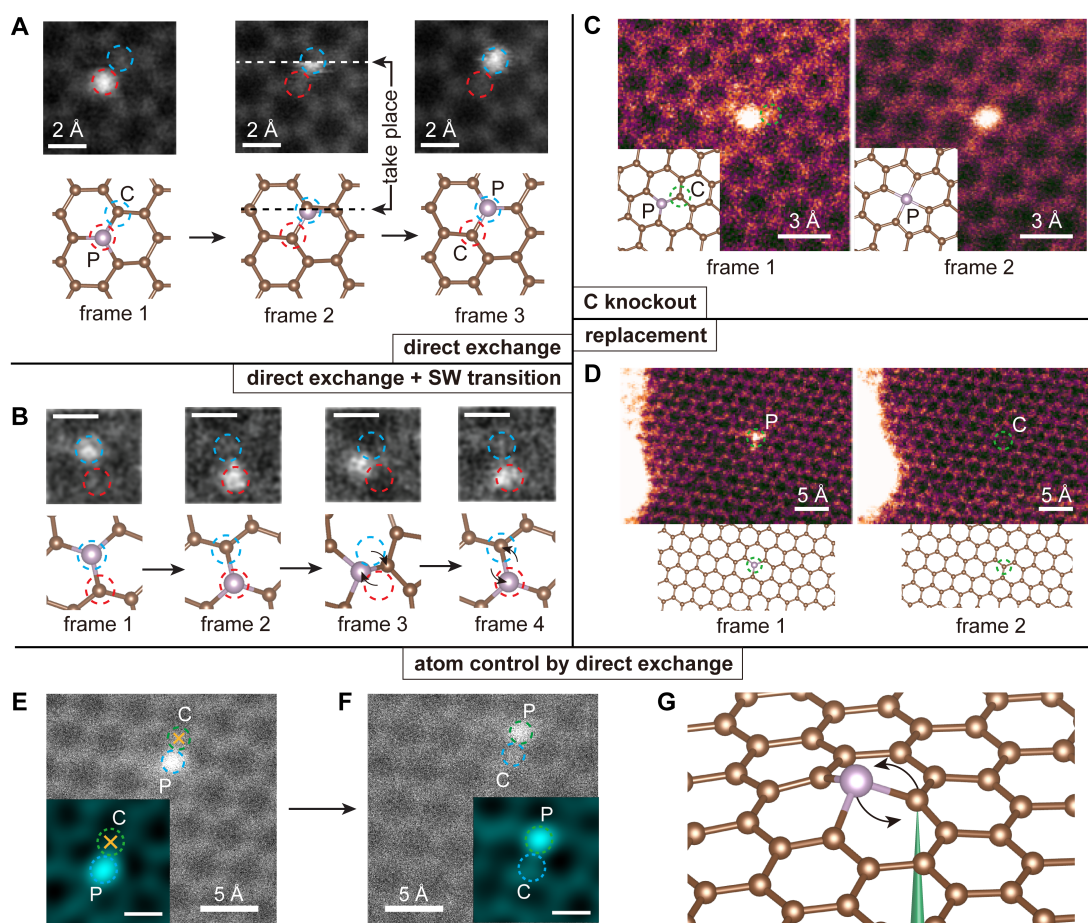


Figure 2-5: Illustration of competing experimental P dopant dynamics in graphene and its control.

transformed into two pairs of 5- and 7-membered rings (55-77 structure hereafter). The 55-77 structure is only stable for less than 0.2 second before reverting back to hexagons (frame 3 to 4) due to the subsequent electron irradiation. In Figure 2-5(C), a three-fold coordinated P (frame 1) turns into four-fold coordinated (frame 2) when the PKA is knocked out by the electron beam. Once this happens, we find the P can no longer be manipulated. In Figure 2-5(D), P is replaced by C, which is the most commonly observed outcome of P impurities-in stark contrast to Si, which are almost never removed or replaced. It should be noted that we never observed a phosphorous being simply knocked out leaving a vacancy behind, consistent with the prediction that its knockout cross section being several orders of magnitude smaller than that of the lighter C atoms.

As a basic step toward controlling the P dopant for atomic engineering, a direct exchange is intentionally initialized by targeting the highly focused e-beam at a neighboring C atom. Since the out-of-plane dynamics of the energetic C neighbor are responsible for the change in the structure [12] the outcome of the exchange can be controlled by selecting the PKA among the three possible carbon neighbors. The initial position of the P dopant is shown in Fig. 1E. The yellow crosses indicate where the electron beam is parked for 10 s, and afterwards, a second frame is immediately captured, shown in Fig. 1F. As a result, the P atom hops site as directed, but this occurred only after 68 ineffective ten-second spot irradiations (another P jumped after 12 ten-second spot irradiations). Compared to Si impurities, P is much harder to induce direct exchange for (Figure 2-5(A)): irradiating the neighbor C site typically triggers the replacement process (Figure 2-5(D)) instead. We tried to manipulate ten P impurities, two of which jumped, one lost a C neighbor, and seven were replaced by C after on average 22 ± 5 (mean \pm std. err.) 10-second spot irradiations.

To reduce the replacement of the dopant by C, we also used double-layer graphene (Figure 2-6), where atom diffusion on one side is suppressed. It is interesting to observe that the phosphorous dopant in a double-layer graphene is much less likely to be replaced than in monolayer graphene. With a similar dose rate, the P atom was not replaced during our observation (~ 12 minutes), which is more than four times longer

than in single-layer graphene (~ 3 minutes). It should be noted that the difficulty of manipulating P atoms represents a generic challenge in atomic engineering, where a desired configurational outcome is degraded by other unwanted ones. Our paper is specifically focusing on dealing with this issue.

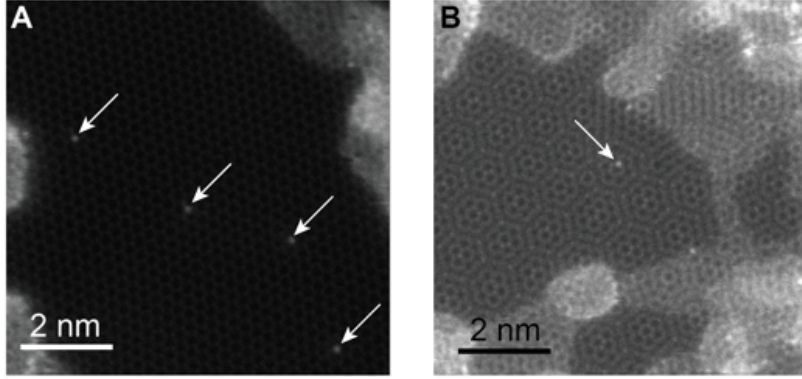


Figure 2-6: STEM MAADF images (raw data) of the single-layer and double-layer graphene area where P dopant atoms are spotted.

To explain these processes, we have performed extensive ab-initio molecular dynamics (abMD) and climbing-image nudged elastic band (cNEB) calculations. With a clear separation of timescales, in particular $\tau_E \ll \tau_I$, it is a reasonable approximation to simulate the configurational change processes on the BO surface assuming each dynamic step evolves according to the Hellman-Feynman forces calculated based on the electronic ground state.

The distribution of various types of dynamics are shown in Figure 2-7(A-C), which corresponds to initial post-collision kinetic energies of the PKA at $E = 15, 16,$ and 17 eV, with the angular space sampled with an interval of 15° for the azimuthal angle φ and 5° for the polar angle θ (up to 25°). Figure 2-7(D-G) are four examples representing different dynamical processes, shown in the order of SW transition, knockout, direct exchange, and unchanged structure. All of these beam-induced dynamics of P dopants are initiated by an out-of-plane momentum imparted on PKA by the backscattering of a single electron, which occurs stochastically with a small probability. The definitions of spherical coordinates θ and φ (momentum direction of the PKA whose energy is E) are plotted in the first frame of Figure 2-7(G), along with

an example of an unchanged structure ($\theta = 25^\circ$, $\varphi = 285^\circ$, with the kinetic energy $E = 15.0$ eV). If the initial velocity is not strictly upwards, but tilted at an angle ($\theta = 20^\circ$, $\varphi = 75^\circ$, $E = 15$ eV in this case), a SW transition occurs (Figure 2-7(D)) [46]. As an example of knockout in Figure 2-7(E), the initial momentum of PKA is tilted toward $\theta = 20^\circ$, $\varphi = 180^\circ$, with E increased to 17.0 eV. Finally, in Figure 2-7(F), an initial PKA velocity perpendicular to the plane ($\theta = 0^\circ$) yields a direct exchange when $E = 17$ eV.

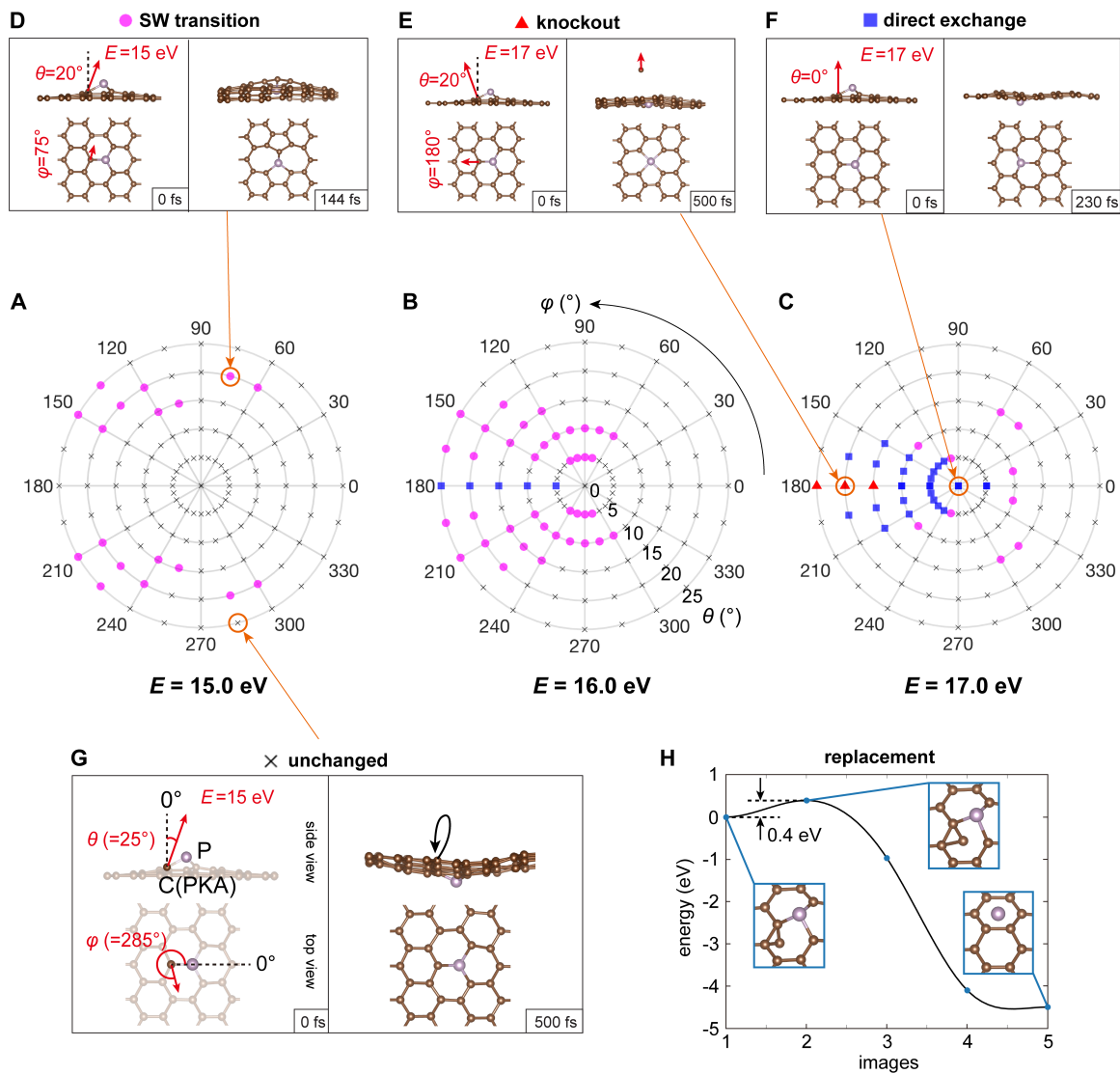


Figure 2-7: Mechanisms of P dopant dynamics in graphene calculated with ab-initio molecular dynamics.

From these plots, several conclusions can be drawn for the phosphorous dopant: (I) a SW transition can be initiated with a lower PKA energy E (starting from 15 eV) than direct exchange. (II) Increasing from 15 to 17 eV, direct exchange gradually becomes the dominant dynamical process. (III) When E reaches around 17 eV, knockouts begin to occur. (IV) Somewhat counterintuitively, direct exchange is easier when the PKA momentum is pointing away from the target P atom ($\varphi = 180^\circ$), instead of pointing toward it ($\varphi = 0^\circ$). As we shall see, these polar plots features are predictable from the PKS theory, from which the relative scattering cross sections of each configurational outcome can be estimated.

The replacement dynamics (Figure 2-5(D)) are due to the free C adatoms on graphene surface. In Figure 2-7(H), our calculation shows that C adatoms can bond stably on a C-C bridge close to the underside of a P site (shown as the initial state). By performing a cNEB calculation, we see that to transit from this initial state to a final state where the P has been replaced by C, the system only needs to cross a 0.4 eV barrier, available thermally or from the 60 keV electron beam [50], and subsequently reducing the potential energy of the system by 4.5 eV.

Comparing different graphene dopants, we found P to hop much less actively in experiment than what has been reported for Si [43]. To explain this, we compare the PKS-predicted energy range of direct exchange for Si, P, as well as Al when assuming a head-on collision ($\theta = 0^\circ$; Figure 2-8(A)). We find that Si clearly covers the greatest energy range, resulting in larger probability of direct exchange than for P. The displacement threshold of the C neighbor of an Al dopant is much lower than for Si and P, so knockout of the PKA is a more likely outcome for Al dopants. In fact, we have observed an Al dopant and its surrounding atoms being displaced by a 60 keV electron beam (Figure 2-8(B)), while we never observe such process for Si or P at the same electron energy. This implies that a lower acceleration voltage (\tilde{E}_e) could help facilitate direct exchange also for Al.

On the contrary, a SW transition is more likely to be observed for a P dopant compared with Si. Related cNEB calculations are shown in Figure 2-8(C). As a broader comparison, we compute six elements, including C, N, B, P, Si, and Al, any

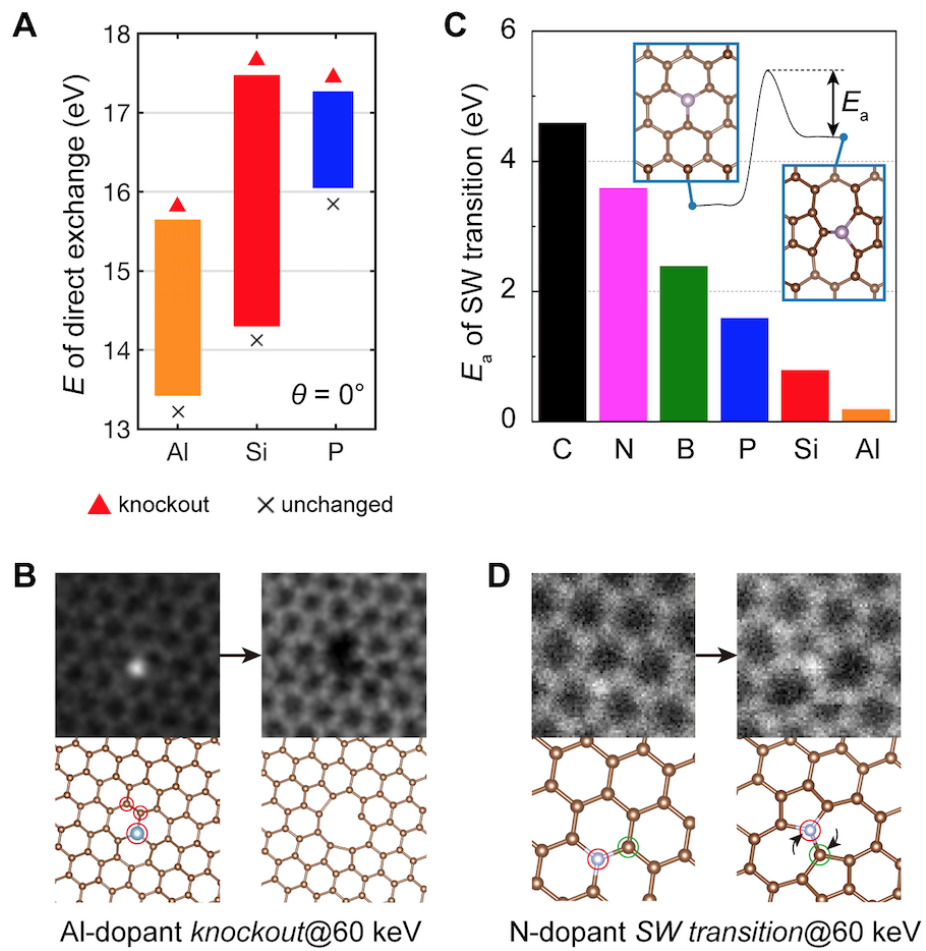


Figure 2-8: Comparison of dynamics of different impurity elements.

of which theoretically could experience a SW transition. To be able to observe the SW transition in STEM, the 55-77 structure must be sufficiently stable to capture an image frame. Its stability is proportional to the depth of the potential energy well of the 55-77 structure (energy barrier between the highest energy transition state and the 55-77 structure), which is given as the activation energy E_a . We note that the cNEB calculation can only provide qualitative ranking, not quantitative characterization of the beam-induced dynamical process, since the electron-imparted momentum is highly localized on the PKA and does not necessarily exactly follow the collective reaction pathway of the minimum energy path. The stability of 55-77 structures follows the order $C > N > B > P > Si > Al$. Among all the dopants we observed, we indeed find that N has the most stable 55-77 structure (Figure 2-8(D)); the single-atom EELS characterization of this particular N dopant can be found in Ref. [51]. Purely thermally, for a pre-exponential factor of 2×10^{12} /s estimated from harmonic analysis in Ref. [52], the Si 55-77 structure back-transformation rate at 300 K is 0.073/s, making such defects (and all the dopants with higher energy barrier) in principle STEM-observable if they are created.

2.5 Primary Knock-on Space

Predicting and comparing the scattering cross sections of different dynamic processes within a unified framework is essential for atomic engineering, so we have developed a formalism, Primary Knock-on Space (PKS). Illustrated on the polar plots in Figure 2-8(A-C), the azimuthal angle φ and polar angle θ correspond to the direction of the momentum of post-collision PKA (Figure 2-9(A)), and the radius of the polar plot represents its kinetic energy E (Figure 2-9(B)). Every point in PKS describes the momentum status of the PKA in terms of its momentum direction and kinetic energy right after collision ($t = \tau_c$), all of which lead to a dynamic outcome which correspond to the points in Figure 2-7(A-C). In Figure 2-9(C), these outcomes are grouped to differently colored blocks represented in three dimensions in PKS. The momentum distribution of knock-on atom after an electron collision has an ovoid profile, whose

shape changes with respect to the energy and direction of an incoming electron and the pre-collisional momentum of the atom. This momentum distribution we conceptualize as a ‘‘Doppler Amplification Effect’’ because small changes in incoming momentum can lead to a much greater change of the outgoing momentum, as illustrated in Figure 2-9(B). Here only atoms vibrating perpendicular to the graphene plane are considered. The Doppler Amplification effect is essential here because our calculation show that if there were no pre-collisional kinetic energy of the atom, there would not be a chance of direct exchange, Stone-Wales transitions, or knockout of a carbon neighbor in the experiments (Figure 2-5). In Figure 2-9(C), the intersection of the colored regions and the ovoid of a vibrating carbon atom (we use $\tilde{E} = 0.5$ eV here for amplified illustration) interacting with a 60 keV electron is projected to the polar plot in Figure 2-5(D), where areas a, b, and c correspond to regions of counterclockwise SW transition, direct exchange, and clockwise SW transition. The existence of these three intersections imply that all of the above dynamic processes are possible when the electron beam is pointing strictly upwards ($\tilde{\theta}_e = 0^\circ$), due to the possibility of the electron scattering to an angle and transferring some lateral momentum [45, 53].

2.5.1 A detailed mathematical derivation of PKS

Every point in PKS describes the momentum status of the PKA in terms of its momentum direction and kinetic energy right after collision, which can be identified by a triplet $\Gamma \equiv (\theta, \varphi, E)$. Similarly, the energy-momentum triplet of a pre-collision electron ($t = 0^-$) will be denoted by $\tilde{\Gamma}_e \equiv (\tilde{\theta}_e, \tilde{\varphi}_e, \tilde{E}_e)$ and that of a pre-collision PKA ($t = 0^-$) will be denoted by $\tilde{\Gamma} \equiv (\tilde{\theta}, \tilde{\varphi}, \tilde{E})$. The PKS differential volume is denoted by $d\Gamma = E^2 d\Omega dE$ where $d\Omega$ is the solid angle of the post-collisional PKA momentum direction, and has unit of eV^3 despite conveying momentum vector-space information (one can think of Γ -space as a transformed momentum space with easy-to-read labels in eV).

The PKS framework involves a two-step process: (1) electron scattering from the nuclear potential of the PKA, denoted ‘‘electron \rightarrow PKA’’ (a zeptosecond-timescale interaction, $\tau_c \sim 10^{-22}$ s) and described by function Q , the PKA momentum resolved

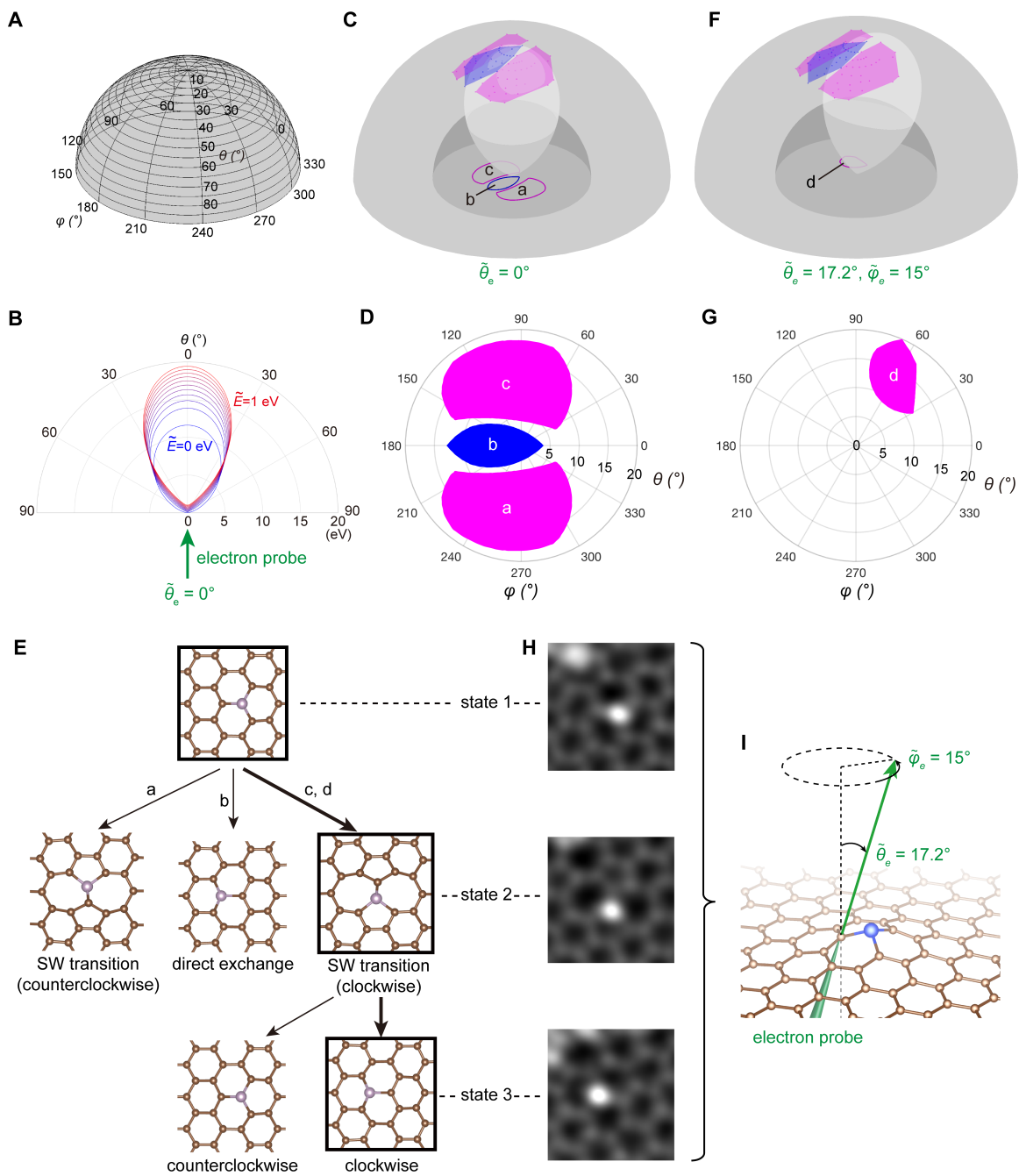


Figure 2-9: Primary Knock-on Space (PKS): a scheme for evaluating relative scattering cross sections of different dynamic processes.

electron differential cross-section; (2) the ensuing dynamics of the PKA, denoted “PKA→configurational change” (a picosecond-timescale interaction, $\tau_1 \sim 10^{-12}$ s) described by P_i , the probability that outcome i will take place. For every energy-momentum triplet Γ in PKS, the outcome functions $P_i(\Gamma)$ describe the probability that such a scattering event leads to an outcome configuration of unchanged ($i = 0$), direct exchange ($i = 1$), SW transition ($i = 2$), knockout ($i = 3$), etc., which is crystal-structure dependent, and with $0 \leq P_i(\Gamma) \leq 1$, $\sum_i P_i(\Gamma) = 1$. Thermal and quantum perturbations of the surrounding crystal structure can smear the branching rates and make P_i neither 1 nor 0, but because E has a much larger magnitude than such surrounding fluctuations, there tends to be a dominant outcome $c(\Gamma) \equiv \arg \max_i P_i(\Gamma)$ for every Γ (c stands for “configurational outcome” denoted by different colors). For example, if direct exchange is the most probable outcome at Γ , then $c(\Gamma) = 1$; if SW transition dominates at Γ , then $c(\Gamma) = 2$, etc. We will use $c(\Gamma)$ to partition the PKS into different color blocks in the 3D visualization scheme shown in Figure 2-9(C) (we use blue color for $i = 1$, magenta for $i = 2$, etc.). Also, $c(\Gamma) = 0$ for regions where recovering to the same configuration is the dominant outcome. Different total cross sections of dynamic processes can be calculated considering the following two consecutive processes:

“Electron→PKA” process: We introduce an intermediate function $Q(\Gamma; \tilde{\Gamma}_e)$, which has units of barn/eV³, to describe the probability that a single penetrating electron can eject the PKA into a particular differential PKS volume $d\Gamma$ (units of eV³) by impinging on the corresponding impact-parameter differential area $d\sigma = Q(\Gamma; \tilde{\Gamma}_e)d\Gamma$. Q is essentially a probability density distribution, partly due to the impact-parameter dependence of the electron-PKA collision, and partly due to the probabilistic nature of $\tilde{\Gamma}$, the pre-collision PKA momentum, which has been shown to be significant and important [47, 54]. Q can be computed as

$$Q(\Gamma; \tilde{\Gamma}_e) = \int d^3\tilde{\Gamma} \times \tilde{P}(\tilde{\Gamma}) \times q(\Gamma, \tilde{\Gamma}; \tilde{\Gamma}_e), \quad (2.26)$$

where $\tilde{P}(\tilde{\Gamma})$ is the probability distribution of PKA momentum before collision ($t = 0^-$) [47, 55], and is its differential volume. The function $q(\Gamma, \tilde{\Gamma}; \tilde{\Gamma}_e)$ describes the energy-momentum resolved cross section of PKA parameterized by $\tilde{\Gamma}$:

$$q(\Gamma, \tilde{\Gamma}; \tilde{\Gamma}_e) \equiv \frac{1}{E^2} \frac{d^2\sigma}{d\Omega dE} = \frac{1}{E^2} \frac{d\sigma}{d\Omega}(\Gamma, \tilde{\Gamma}; \tilde{\Gamma}_e) \times \delta \left[E - f(\theta, \phi, \tilde{\Gamma}; \tilde{\Gamma}_e) \right], \quad (2.27)$$

where $\frac{d\sigma}{d\Omega}(\Gamma, \tilde{\Gamma}; \tilde{\Gamma}_e)$ is the angular resolved differential cross section of electron-atom scattering derived from McKinley-Feshbach formalism [47, 56],

$$\sigma(\theta) = \sigma_R \left[1 - \beta^2 \sin^2\left(\frac{\theta}{2}\right) + \pi \frac{Ze^2}{\hbar c} \beta \sin(\theta/2) \left(1 - \sin\left(\frac{\theta}{2}\right)\right) \right] \quad (2.28)$$

and

$$\sigma_R = \left(\frac{Ze^2}{8\pi\epsilon_0 m_0 c^2} \right)^2 \frac{1 - \beta^2}{\beta^4} \csc^4(\theta/2). \quad (2.29)$$

which describes the scattering probabilities of PKA with respect to its outgoing angles and energy. The delta function in energy is the result of energy-momentum conservation and is independent of the details of the nuclear potential. The function f defines the energy contour of PKA with respect to the outgoing angles θ, φ given the status of incident electron $\tilde{\Gamma}_e$ and pre-collision PKA, $\tilde{\Gamma}$. We use a relativistic treatment to obtain f as shown in the following equation:

$$f(\theta, \varphi, \tilde{\Gamma}; \tilde{\Gamma}_e) = E_{\max} (\sin \tilde{\theta}_e \cos \tilde{\varphi}_e \cos \varphi \sin \theta + \sin \tilde{\theta}_e \sin \tilde{\varphi}_e \sin \varphi \sin \theta + \cos \tilde{\theta}_e \cos \theta)^2 + \Delta E_{\text{vib}}(\theta, \varphi, \tilde{\Gamma}), \quad (2.30)$$

where the first term accounts for the ovoid without vibration ($\tilde{E} = 0$), and the second is a correction to the first term by considering the pre-collision status of PKA ($\tilde{\Gamma}$). The above equation can be simplified for head-on collision ($\tilde{\theta}_e = 0$) and $\tilde{E} = 0$:

$$f(\theta, \varphi, \tilde{E} = 0; \tilde{\theta}_e = 0) = E_{\max} \cos^2 \theta. \quad (2.31)$$

The $q(\Gamma, \tilde{\Gamma}; \tilde{\Gamma}_e)$ function, parametrized by the incident electron energy \tilde{E}_e and mo-

momentum direction $\tilde{\theta}_e$, $\tilde{\varphi}_e$, describes the scattering from the nuclear potential, and thus does not depend on the crystal structure.

“PKA→configurational change” process: The total cross section of a dynamic process i can then be computed by integrating Q in equation (2.26) weighted by outcome function P_i over the whole PKS:

$$\sigma_i(\tilde{\Gamma}_e) = \int d^3\Gamma \times P_i(\Gamma) \times Q(\Gamma; \tilde{\Gamma}_e), \quad (2.32)$$

where $d^3\Gamma \equiv E^2 \sin \theta dE d\theta d\varphi$ is the PKS differential volume element for post-collision PKA. The cross sections of different dynamic processes are functions of $\tilde{\Gamma}_e$, indicating that the probabilities of different dynamics can be tuned by the energy of electron (\tilde{E}_e), or by the incident angles ($\tilde{\varphi}_e, \tilde{\theta}_e$) with respect to the sample, which can be tuned by tilting the beam or the sample (Figure 2-10). These are the primary control variables of atomic engineering, along with the selection of the PKA.

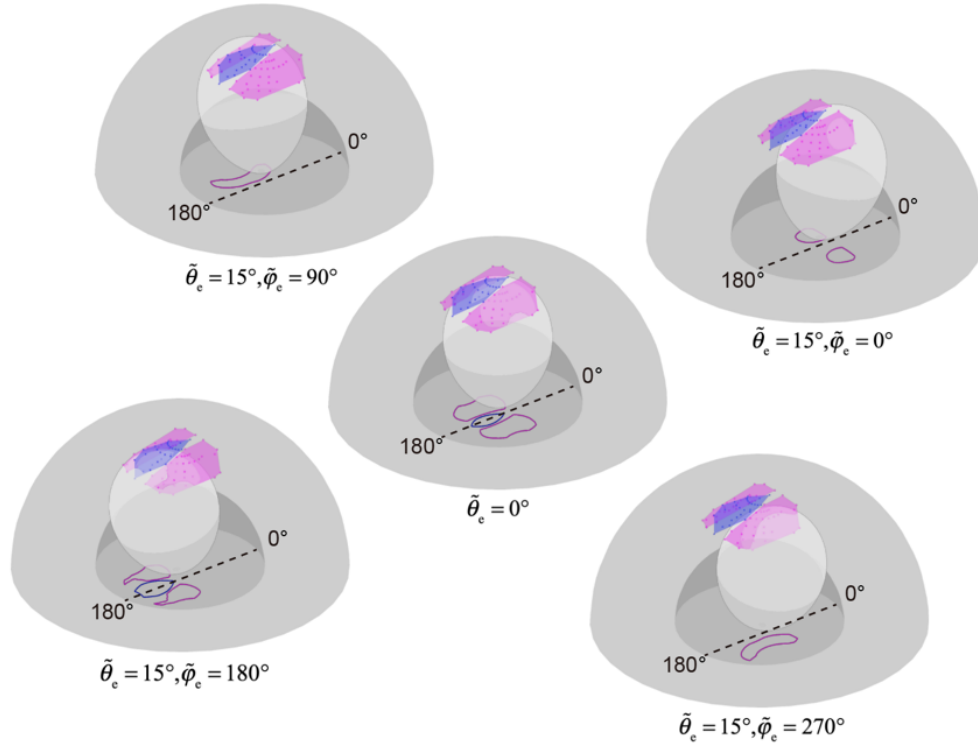


Figure 2-10: The selective dynamics by tilting electron beam.

In computer-controlled atomic engineering, in evaluating equation (2.32), although $Q(\Gamma; \tilde{\Gamma}_e)$ has many dependent variables and equations (2.26), (2.27) look complicated, they are analytical integrals and thus can be evaluated on-the-fly. $P_i(\Gamma)$, however, are crystal- and material-dependent, and need to be pre-computed with expensive *ab initio* calculations, and tabulated or machine-learned [57] for efficient evaluation of equation (2.32).

For simplicity, in the graphical illustrations so far, the “PKA→configurational change” dynamics are assumed to be deterministic, making $P_i(\Gamma)$ either 0 or 1, without any smearing at the boundaries. This is reflected in Figure 2-9(C) as the sharp boundaries of the PKS regions, where the probability of configurational outcome i is 1 within the boundary, and is 0 everywhere else. On the other hand, the contour of $\delta \left[E - f(\theta, \phi, \tilde{\Gamma}; \tilde{\Gamma}_e) \right]$ is an ovoid with infinitely thin shell in PKS. The electron cross section of certain configurational outcome, σ_i , can thus be visualized easily in this limit: the intersection areas between the ovoid and the $c(\Gamma) = i$ regions represent the part of PKS space that can induce certain configurational change i , which is then convoluted with $d\sigma/d\Omega$ to get the total cross section for each of them.

2.5.2 Doppler amplification effect

To complicate the picture a bit, however, for a quantitative description of knock-on effects, it has been shown that the pre-collisional momentum $\tilde{\Gamma}$ of the PKA is significant and important [47, 54], due to what we may conceptualize as a “Doppler Amplification Effect” on Γ .

To illustrate this with an approximate example (Figure 2-11), the outgoing velocity, \mathbf{v} , of a PKA with pre-collisional vibrational velocity, $\tilde{\mathbf{v}}$, can be well approximated by $\mathbf{v} \approx \mathbf{v}_0 + \tilde{\mathbf{v}}$, where \mathbf{v}_0 is the post-collisional velocity of a static PKA. Squaring the two sides yields the energy equation $E \approx E_0 + M\mathbf{v}_0 \cdot \tilde{\mathbf{v}} + \tilde{E}$. A small change in \tilde{E} may result in up to $\sim 10\times$ change in E due to the second term $M\mathbf{v}_0 \cdot \tilde{\mathbf{v}}$, since \mathbf{v}_0 is significantly larger than $\tilde{\mathbf{v}}$ (because \mathbf{v}_0 corresponds to energy of 10 eV whereas corresponds to energy of ~ 0.1 eV). So a change as small as 0.1 eV due to thermal and quantum zero-point fluctuations in the pre-collision nuclear kinetic energy can

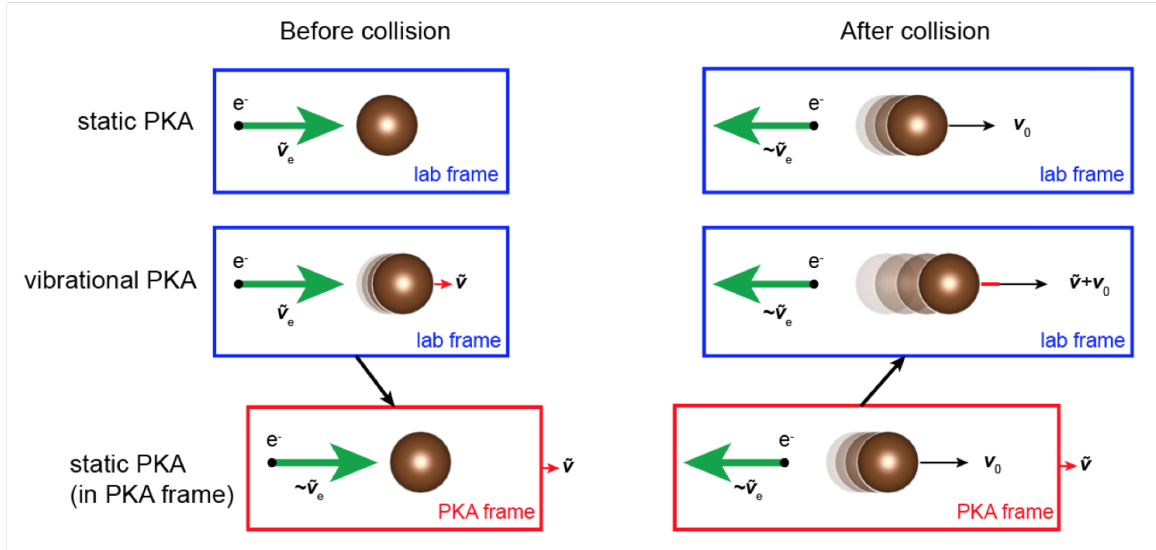


Figure 2-11: Derivation of final velocity of PKA when it is not static before interaction, by transitioning between lab frame and center of mass frame.

change the PKA post-collision kinetic energy by as much as 1 eV, which subsequently can significantly alter the dynamical outcome. In momentum space, it is shown that the in-plane vibration also contributes to the amplification effect. This necessitates a careful integration treatment in equation (2.26), where the infinite-thin shelled differential cross-section $q(\Gamma, \tilde{\Gamma}; \tilde{\Gamma}_e)$ will be smeared into a Bowling pin-shaped probability density $Q(\Gamma; \tilde{\Gamma}_e)$ that depends on the pre-collisional velocity distribution (Figure 2-12).

Intuitively, Doppler Amplification Effect can be understood in the following way: when atomic nucleus is moving along the incident direction of electron, the reflected electron tends to have a lower energy, just the same as the sound is lower in pitch when reflected from a car moving away. When nucleus is moving toward the electron, after interaction, the reflected electron tends to have higher energy, just like a higher pitch of reflected sound bouncing from a car moving toward the sound source. Whenever the *reflected electron* has a lower energy, due of the conservation of energy, more energy will be transferred to *nucleus*, and vice versa.

Let us consider the most generic picture of a two-body collision between an electron and an atom (Figure 2-12(A)). Again, by writing down the conservation of

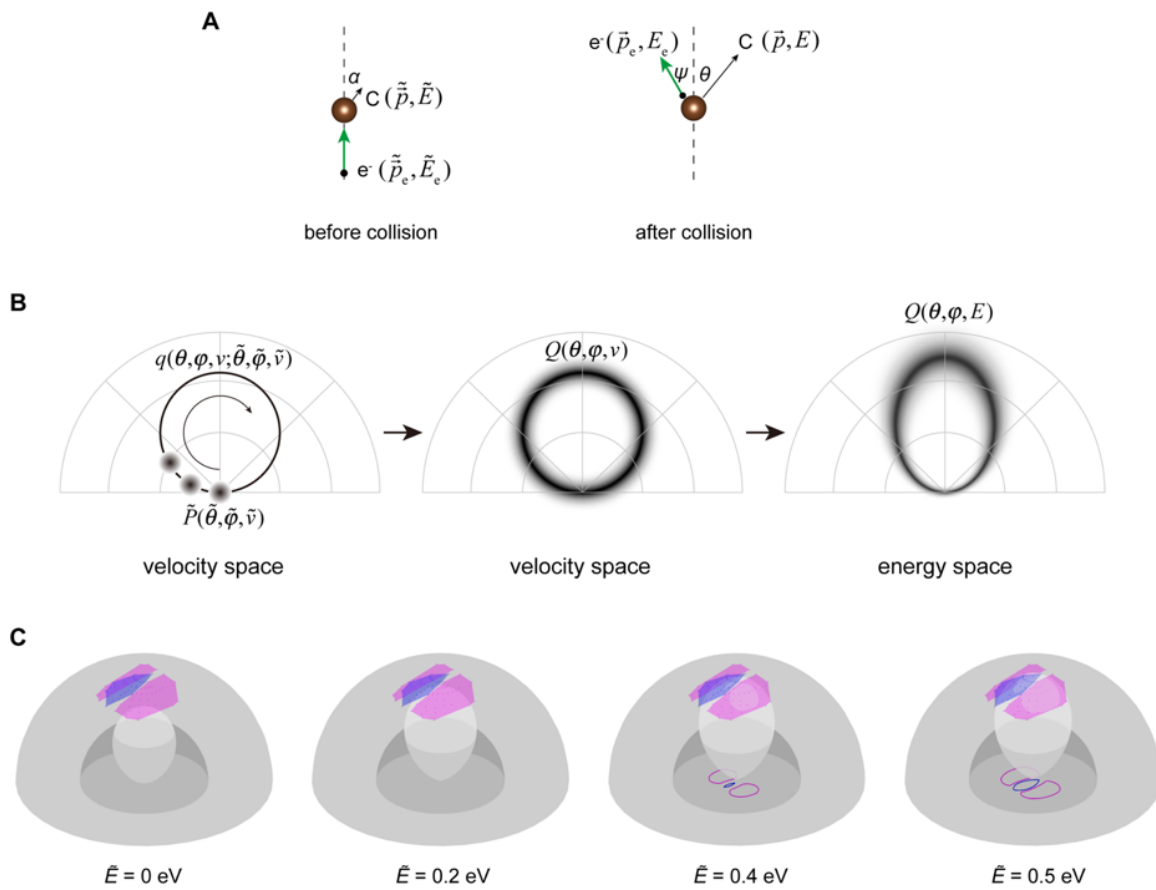


Figure 2-12: The modified ovoid when PKA is not static before interaction.

momentum:

$$\left| \tilde{\vec{p}}_e \right| + \left| \tilde{\vec{p}} \right| \cos \alpha = \left| \vec{p} \right| \cos \theta + \left| \vec{p}_e \right| \cos \psi, \quad (2.33)$$

$$\left| \tilde{\vec{p}} \right| \sin \alpha = \left| \vec{p} \right| \sin \theta + \left| \vec{p}_e \right| \sin \psi, \quad (2.34)$$

and the conservation of energy:

$$\tilde{E}_e + \tilde{E} = E + E_e, \quad (2.35)$$

and by inserting equations (2.5) and (2.6), we get the relation:

$$\begin{aligned} & \frac{1}{c} \sqrt{2\tilde{E}_e E_0 + \tilde{E}_e^2} + \sqrt{2M\tilde{E} \cos^2 \alpha} = \\ & \sqrt{2ME} \cos \theta \pm \frac{1}{c} \sqrt{2\tilde{E}_e E_0 + \tilde{E}_e^2} \left[1 - \frac{c^2}{2\tilde{E}_e E_0 + \tilde{E}_e^2} \left(\sqrt{2ME} \sin \theta - \sqrt{2M\tilde{E} \sin^2 \alpha} \right)^2 \right]^{1/2}. \end{aligned} \quad (2.36)$$

To simplify the picture, let us only consider an atom vibrating in the same direction as the electron before collision, in which case $\alpha = 0$. By solving for E with respect to the angle θ , we now get

$$\begin{aligned} \sqrt{E} = & \left[\sqrt{\frac{2\tilde{E}_e E_0 + \tilde{E}_e^2}{2Mc^2}} + \sqrt{\tilde{E}} \right] \cos \theta \\ & \pm \sqrt{\left[\sqrt{\frac{2\tilde{E}_e E_0 + \tilde{E}_e^2}{2Mc^2}} + \sqrt{\tilde{E}} \right]^2 \cos^2 \theta - \frac{\sqrt{2M\tilde{E}(2\tilde{E}_e E_0 + \tilde{E}_e^2)} + M\tilde{E}c}{Mc}} \end{aligned} \quad (2.37)$$

where the valid range of θ is defined by

$$\left[\sqrt{\frac{2\tilde{E}_e E_0 + \tilde{E}_e^2}{2Mc^2}} + \sqrt{\tilde{E}} \right]^2 \cos^2 \theta - \frac{\sqrt{2M\tilde{E}(2\tilde{E}_e E_0 + \tilde{E}_e^2)} + M\tilde{E}c}{Mc} \geq 0. \quad (2.38)$$

The Figure 2-9(B) is obtained by changing the initial atom vibrational energy \tilde{E} .

Post-collision, once over a short period of τ_E , the PKS momentum distribution $Q(\Gamma; \tilde{\Gamma}_e)$ will be convoluted with $P_i(\Gamma)$, a crystal-dependent quantities that one can

pre-compute with DFT that integrates the evolution of atom trajectories on the ground-state BO surface (since we are beyond τ_E). The overlap of $Q(\Gamma; \tilde{\Gamma}_e)$ (nuclear collisional kinematics) and $P_i(\Gamma)$ (crystal-structure dependent transition probability) in PKS space gives the net rate of configurational change ($\rightarrow i$), after which the correlated atomic momenta dephase and the momenta correlation information gets lost, leaving only heat. All these happen (or not) long before the next electron penetrates the system, and the system configuration evolves ($i \rightarrow i' \rightarrow i'' \rightarrow \dots$) without carrying the detailed phase information about atomic momenta, so an uncorrelated probability distribution function about PKA momentum $\tilde{P}(\tilde{\Gamma})$ is all we need for characterizing this driven system.

The effect of in-plane vibration to the final transferrable energy can be rationalized by an observation frame-translation effect. Consider pre-collisional velocity $\tilde{\mathbf{v}}$ and post-collisional velocity \mathbf{v} of the PKA. We expect that, order-of-magnitude wise, $M\tilde{\mathbf{v}} \cdot \tilde{\mathbf{v}}/2 \sim 0.1$ eV and $M\mathbf{v} \cdot \mathbf{v}/2 \sim 10$ eV, where M is the mass of the PKA. Thus \mathbf{v} is about $10\times$ the size of $\tilde{\mathbf{v}}$. Let us first consider a reference case of $\tilde{\mathbf{v}} = 0$ and solve for $\mathbf{v} \equiv \mathbf{v}_0$ for a given impact parameter b , and then “turn on” finite but small $\Delta\tilde{\mathbf{v}}$. Since a 60 keV electron moves with the speed 1.3377×10^8 m/s (about 45% of light speed), and $\Delta\tilde{\mathbf{v}}$ is only of the order 10^3 m/s, seen in a translating frame of velocity $\Delta\tilde{\mathbf{v}}$ with respect to the lab frame, the incoming electron velocity is barely changed (60 keV \rightarrow 59.999 keV), so for the same impact geometry, the outgoing PKA velocity in this co-translating frame is nearly \mathbf{v}_0 . Yet, when transforming back from the translating frame to the lab frame, we need to add back $\mathbf{v}_0 \rightarrow \mathbf{v}_0 + \Delta\mathbf{v}$, so we obtain

$$\begin{aligned}
E_0 \equiv \frac{M\mathbf{v}_0 \cdot \mathbf{v}_0}{2} &\rightarrow E \approx \frac{M(\mathbf{v}_0 + \Delta\tilde{\mathbf{v}}) \cdot (\mathbf{v}_0 + \Delta\tilde{\mathbf{v}})}{2} \\
&= \frac{M\mathbf{v}_0 \cdot \mathbf{v}_0}{2} + \frac{M\Delta\tilde{\mathbf{v}} \cdot \Delta\tilde{\mathbf{v}}}{2} + M\mathbf{v}_0 \cdot \Delta\tilde{\mathbf{v}} = E_0 + \tilde{E} + M\mathbf{v}_0 \cdot \Delta\tilde{\mathbf{v}}. \quad (2.39)
\end{aligned}$$

Thus from the second term, we get a baseline sensitivity of 1 (if PKA’s pre-collision energy is 0.1 eV, this part will be inherited directly), but the third term can give a much larger sensitivity of $10\times$ due to the larger magnitude of \mathbf{v} compared to the size of $\tilde{\mathbf{v}}$, and this amplification sensitivity is also directional ($10\times$ or $-10\times$ if parallel or

anti-parallel fluctuation, $0\times$ if transverse fluctuations) like in Doppler effect.

2.5.3 Manipulation decision tree

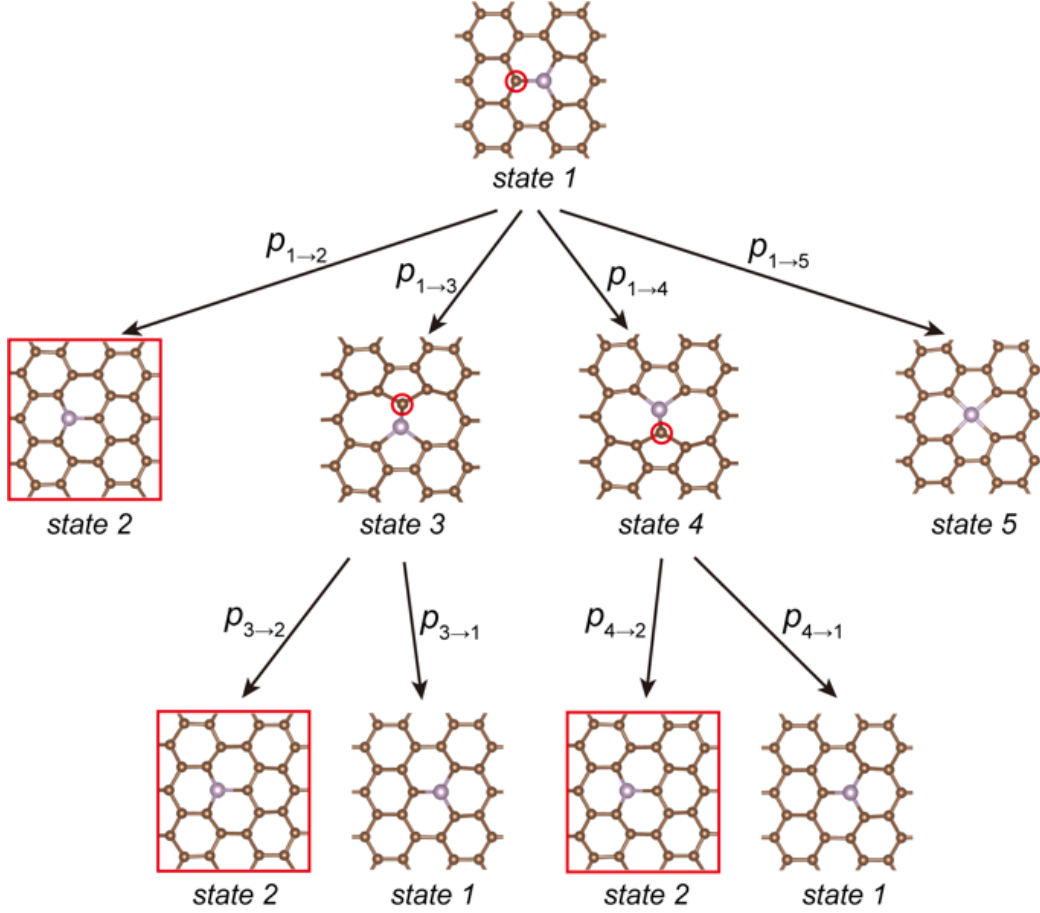


Figure 2-13: A decision tree for engineering atom configurations in doped graphene.

In atomic engineering, a decision tree is used to show the possible paths of evolution (Figure 2-13), with its root node indicating the initial structure, and the child nodes indicating the next possible structures with different branching probabilities. The probability of each dynamic process can be obtained as

$$p_{i \rightarrow k}(\tilde{\Gamma}_e) = \frac{\sigma_{i \rightarrow k}(\tilde{\Gamma}_e)}{\sum_k \sigma_{i \rightarrow k}(\tilde{\Gamma}_e)}. \quad (2.40)$$

We can therefore maximize the probability of a specific configuration change by

choosing a combination of angles that maximizes the probability of desired branches while minimizing that of undesired ones. In our P-doped sample, the root trifurcates into three different paths, corresponding to the three different dynamic processes (Figure 2-9(E)). By using the PKS formalism above and taking the mean squared velocity of the carbon atom to be $3.17 \times 10^5 m^2 s^{-2}$ [47] or $\tilde{E} = 0.02$ eV, we can calculate the relative probability between the SW exchange and direct exchange as ~ 63.4 . Experimentally, we find this number to be somewhat higher at ~ 224 (11.2 barn / 0.05 barn, as found in Table 1). Apart from the approximation we have done in our calculation, DFT/MD overestimates the energy required for inducing dynamics by about 10% [29,56], partly due to possible inaccuracies in the description of bond-breaking in standard (semi-)local DFT [58], and the scheme we have constructed here does not consider electronic excitations. For these reasons, we considered only relative probabilities in the PKS above. Further improvements in theoretical modeling are needed before quantitative predictions are possible for impurity sites in graphene [29] and to account for the in-plane vibration components of the C atoms. However, we want to stress here that PKS correctly predicts that the SW transition has a much higher probability than direct exchange, whereas static in-plane transition paths calculated with cNEB cannot rationalize the difference between the two processes.

To further experimentally test our theory, we tilted a Si-doped sample so that the electron beam was incident at a specific angle ($\tilde{\theta}_e = 17.2^\circ$, $\tilde{\varphi}_e = 15^\circ$, determined from the calibrated double-tilt sample holder; due to their similar covalent size and bonding, we expect the relative positions of outcome functions of threefold Si and P impurities to be similar). Based on our calculations, with such a tilt, the direct exchange and the counterclockwise SW transition will be totally suppressed, leaving only clockwise SW transition active (Figure 2-9(F, G)). In this proof-of-principle experiment, we indeed observed only clockwise SW transitions (Figure 2-9(H)), demonstrating control of this configurational outcome. Thereafter, from the 55-77 structure back to the honeycomb lattice, clockwise SW transition is again the only active dynamic process (Figure 2-14).

The long-term vision of Atomic Engineering is to precisely position individual

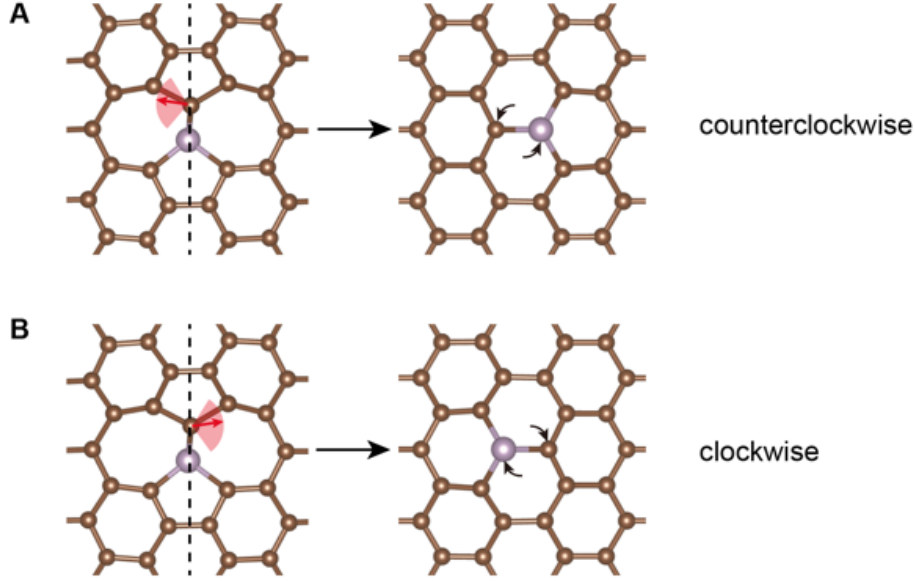


Figure 2-14: The selective dynamics from 55-77 structure back to honeycomb when beam tilted.

atoms with desired internal states including the nuclear spin, image and control atomic assemblies from 1 to 1000 atoms, and use precisely controlled atoms and their electronic/nuclear states for devices such as atomic clock and memory. Successful atomic engineering comes from understanding two parts: (I) how the desirable local configurational changes can be induced to increase the speed and success rate of control, and (II) how to scale up these basic unit-processes into feasible structural assemblies of 1-1000 atoms to produce the desired functionality. In this paper we focused on the first part by surveying the single-step dynamics of graphene dopants, primarily phosphorus, caused by electron irradiation both in experiment and simulation, and developed a theoretical scheme for describing the probabilities of competing configurational outcomes, through the post-collisional momentum vector of the PKA. However, a brief description of the second part is also warranted.

What one would want is to arrive at a pre-designed configurational state $i_{\text{final}} \equiv \{r_n\}$ of the atoms as quickly as possible, through a series of collisions with narrowly focused electrons, which are known to possess enough energy to displace atoms in the radiation damage community [59], but exploited here in a controlled fashion to

bias the configurational evolution, some of which may conserve mass locally and some of which may not. We start with an initial configurational state i_{initial} that is precisely imaged, and wish to travel across intermediate configurations $\dots \rightarrow i \rightarrow i' \rightarrow i'' \rightarrow \dots$ and finally arrive at i_{final} , similar to playing Rubik’s Cube but with probabilities. One obviously must balance “risk” against “speed” in playing this game, since there could exist trap states i_{trap} that severely delays the arrival to i_{final} , or even make achieving i_{final} impossible (for example, four-fold coordinated P is a trap state with 60 keV e-beam, since we found it is no longer possible to further alter the configuration once there). Through the PKS formalism, we see that we can affect i through the following control variables: (a) choosing the PKA atom and the e-beam spot center, (b) choosing FWHM of the e-beam and the beam dose, (c) choosing \tilde{E}_e , (d) choosing $(\tilde{\theta}_e, \tilde{\varphi}_e)$ by tilting the sample or the beam, (e) choose the temperature of the environment which can effectively change the doping level of sample, with the constraint that one must also be able to simultaneously image the sample for feedback control. The probabilistic nature of this tree-traversal game makes it similar also to chess. Computational prediction of the branching ratios and the absolute transition-rate, even if approximate, would be key for any kind of engineering optimization of the total risk/speed trade-off. Conceivably, one could apply machine learning [57] and artificial intelligence to understanding the unit-processes, as well as the assembly process, in the future. However, first-principles theory has at this stage been demonstrated to be tremendously helpful.

Specifically in this chapter, we have categorized four types of electron-induced dynamics of atomic dopants on graphene and constructed a scheme for controlling them. By explaining the mechanisms for each process by first-principles calculations, we provide a convenient categorization for generic dopant dynamics. We have demonstrated the possibility of electron-beam manipulation of P, and selectively induced directional Stone-Wales transitions of Si. A vector-space theory (Primary Knock-on Space, PKS) is proposed for calculating the relative ratio of scattering cross sections between different configurational outcomes (branching probabilities in a decision tree). The two main ingredients of this theory, the outcome functions and the momentum-resolved

differential cross-sections, are assessed and numerically computed by *ab initio* molecular dynamics and analytical relativistic electron collision kinematics, respectively. A “Doppler Amplification Effect” is discussed whereby small change in pre-collisional PKA momentum results in larger change in PKS momentum due to momentum conservation.

The PKS theory is developed based on the fortunate separations of timescales of relativistic electron collision ($\tau_c \sim 10^{-22}$ s), electronic excitation (a penetration event, $\tau_e \sim 10^{-18}$ s), collective post-penetration electronic relaxation ($\tau_E \sim 10^{-15}$ s), ionic trajectory ($\tau_I \sim 10^{-12}$ s) leading to configurational change, and the frequency of such penetrations ($\tau_p \sim 10^{-9}$ s). While momenta will eventually be dephased after τ_I , what the PKA momentum vector was and how this vector may evolve up to τ_I are essential, so this is a truly dynamical problem. Up to τ_c , we have a relativistic collision problem that is PKA nucleus dependent but crystal-independent. The physics revealed and the computational/analytical framework developed in this paper is general, and can further help develop techniques for controlling single-atom dynamics in 3D materials [44], and ultimately, upscaling manipulations of multiple atoms to assemble 1-1000 atoms with high speed and efficacy.

2.6 Discussion on Space Charge

The whole analysis above is based upon the discussion of a single electron interacting with an atom when calculating the energy-momentum resolved differential cross section (the ovoid). However, it is quite natural to question the validity of assuming only one electron exists during the interaction. The following derivation is used for proving that two electrons cannot act on the same atom when traveling from the electron source to the sample. Consider two electrons, each with mass m_e and with charge of $-e$, repel each other with potential

$$V(r) = \frac{e^2}{4\pi\epsilon_0 r} \tag{2.41}$$

where ϵ is the vacuum permittivity, and r is the distance between the two electrons. The repelling forces exert on these two electrons pointing toward opposite directions are equal in magnitude:

$$F(r) = -\Delta V = \frac{e^2}{4\pi\epsilon r^2}. \quad (2.42)$$

Let's suppose at $t = 0$, we have $r = r_0$, and in a stationary frame where the electron on the left is at $-r_0/2$, and electron on the right side is at $r_0/2$. We have

$$m_e \frac{d^2x}{dt^2} = \frac{m_e}{2} \frac{d^2r}{dt^2} = \frac{e^2}{4\pi\epsilon r^2}. \quad (2.43)$$

so to simplify,

$$\frac{d^2r}{dt^2} = \frac{e^2}{2\pi m_e \epsilon_0 r^2}. \quad (2.44)$$

which is a nonlinear second order differential equation. Changing the variable gives

$$\frac{dr}{dt} \frac{d^2r}{dt^2} = \frac{d}{dt} \left(\frac{1}{2} \left(\frac{dr}{dt} \right)^2 \right) = -\frac{e^2}{2\pi m_e \epsilon_0} \frac{dr^{-1}}{dt} \quad (2.45)$$

$$\frac{1}{2} \left(\frac{dr}{dt} \right)^2 = \frac{e^2}{2\pi m_e \epsilon_0} (r_0^{-1} - r^{-1}) \quad (2.46)$$

$$\frac{dr}{dt} = \sqrt{\frac{e^2}{\pi m_e \epsilon_0} (r_0^{-1} - r^{-1})} \quad (2.47)$$

so

$$t = \sqrt{\frac{\pi m_e \epsilon_0 r_0^3}{e^2}} \int \frac{d\tilde{r}}{\sqrt{1 - \tilde{r}^{-1}}} = \sqrt{\frac{\pi m_e \epsilon_0 r_0^3}{e^2}} [\sqrt{\tilde{r}(\tilde{r} - 1)} + \ln(\sqrt{\tilde{r}} + \sqrt{\tilde{r} - 1})], \quad (2.48)$$

where $\tilde{r} = r/r_0$. If the initial distance is on the order of one atom, i.e. 1\AA , the reduced timescale $\sqrt{\frac{\pi m_e \epsilon_0 r_0^3}{e^2}} = 3.14 \times 10^{-17}\text{s}$, we can get the following plot of time t as a function of \tilde{r} .

It takes about 1 ns for electrons to travel from the electron source to sample, so at the time when these two electrons reaches the sample, they are already $r = 3.2$ mm away from each other, which makes it impossible to focus them onto the same atom. From the above plot, we find that for large $\tilde{r} = r/r_0$, it can be well approximated by

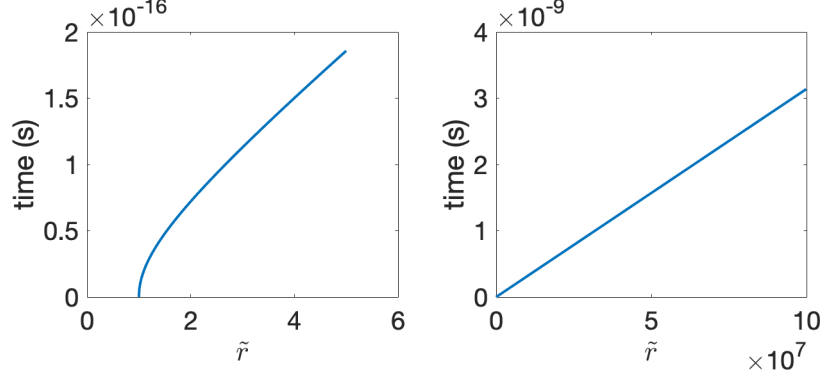


Figure 2-15: Elapsed time as a function of $\tilde{r} = r/r_0$ when $r_0 = 1 \text{ \AA}$. Left panel: when \tilde{r} is close to 1; right panel: when $\tilde{r} \gg 1$, which becomes a linear function.

the leading order

$$t \approx \sqrt{\frac{\pi m_e \epsilon_0 r_0^3}{e^2}} \frac{r}{r_0}. \quad (2.49)$$

A cold field emission gun used inside the microscope is usually on the order of 5 nm [60], therefore, r_0 can be at a maximum of 5 nm. This lead to a minimum of $r = 0.14 \text{ nm}$, which is still way larger than the size of atom. Therefore, we conclude that having two electrons coming to the same atom at the same time is impossible.

2.7 The Influence of Excited States on Outcome Functions

Another factor that needs to be concerned is that while we are simulating the outcome functions of C atom above, we assumed ground state electronic structures in each MD step. This is considered to be a very good approximation, as the timescale of electronic structure relaxation of graphene (1 fs) is much less than the dynamic process of C and P atoms (0.2 ps). However, it is still unclear how dopant atoms could influence the dynamics of electronic structure of graphene. It should be noted that by assuming a pure ground state evolution in MD, we cannot reproduce the SW transition of N-doped graphene. This elucidates that even in this graphene-based system, the timescale of some other processes might be on par with the atom dynamics. One reason might be

Table 2.1: Lifetime of inelastic excitations in some common 2D materials.

Materials	Lifetime (s) [62]			
	Core hole	Valence hole	Plasmon	Phonon
Graphene	10^{-14}	10^{-15}	10^{-13}	10^{-12}
MoS ₂	$<10^{-15}$	10^{-12}	10^{-10}	10^{-9}
hBN	10^{-15}	10^{-9}	-	10^{-12}

plasmonic excitation of graphene, which has a lifetime of 20 fs, overlapping with the early stage of atom dynamics [61].

For other systems like hexagonal boron nitride (hBN) [63, 64] and molybdenum disulfide (MoS₂) [65–67], the time duration of excited state has been already proved to be on par or even longer than the atom dynamics [62], listed in Table 2.1.

In the introduction section, we knew that for 160 pA of current, there are in principle 10 electrons in every second that can induce the dynamic processes. From the conclusion of the “Doppler Amplification Effect” section, we know that these 10 effective electrons have to be convoluted to the possibilities of having an atom with enough initial momentum to link the gap between E_{\max} and the minimum initial kinetic energy required for inducing any kind of dynamics. This lowers down the dynamics that can be induced significantly. What is peculiar is that the dynamics of Si dopant inside graphene happens almost every 10 seconds when it is scanned in a 1 nm \times 1 nm area. Of all of these area, the three nearest neighbor of Si dopant takes up a total space of 10%, which in turn means that for each single effective electron that goes across the “dynamics active cross section”, it can induce a dynamic process at a probability of 10%! This clearly contradicts with the fact that there is a huge gap between the ovoid and outcome functions. Therefore, even with a dopant atom inside graphene, assuming ground states for each single dynamic step might not be a good approximation.

2.8 Heat injection from electron beam

As electron exchange energy with graphene sample, it instantaneously (smaller than 1 attosecond) creates a heat source and diffuse away. Mathematically, it is then justified to treat the temperature of graphene as a thermal diffusion problem in 2D with a repetitive heat source acting within a region following a Gaussian shaped geometry (FWHM = 1Å).

Start from the very beginning, the heat equation is

$$\rho c_p \frac{\partial T}{\partial t} - \nabla \cdot (k \nabla T) = \dot{q}_V \quad (2.50)$$

where c_p is the specific heat capacity, ρ is the density of materials, and \dot{q}_V is the volumetric heat source. If thermal diffusivity is defined as $\alpha = k/c_p\rho$, and the heat source is treated as a delta function, the heat equation in our specific problem turns into

$$\frac{\partial u}{\partial t} - \alpha \nabla^2 u = \delta(\mathbf{r} - \mathbf{r}_0) \quad (2.51)$$

where \mathbf{r}_0 is the position of the electron probe on sample. This turns into what is called a "fundamental solution/heat kernel" problem, where general heat transfer problem can be simplified to be a Greens Function problem. The general solution of a heat equation in d -dimension is

$$\Phi(\mathbf{r}, t) = \frac{1}{(4\pi\alpha t)^{d/2}} \exp\left(-\frac{\mathbf{x} \cdot \mathbf{x}}{4\alpha t}\right) \quad (2.52)$$

and the temperature follows

$$T(\mathbf{r}, t) = \int \Phi(\mathbf{r} - \mathbf{r}', t) g(\mathbf{r}') d\mathbf{r}' \quad (2.53)$$

In our case, the electron can be treated as a point source, so the temperature distribution should have the exact form in equation 2.53. For graphene, $d = 2$, and the temperature drops with respect to $T \propto 1/t$. If we assume that the time interval of electron coming down to the sample at a constant time interval, and if we assume

that the thermal wave packet diffuse as an independent manner from each other, then at a specific time point t_n (with a time interval of t_0), the temperature accumulated on the electron spot is

$$T(\mathbf{r}_0, t_n) = \sum_n \frac{1}{nt_0} = \frac{1}{t_0} \sum_n \frac{1}{n} \quad (2.54)$$

which diverges as function $f(n) = \ln n$ when $t \rightarrow +\infty$. On the contrary, we never observed such temperature divergence in experiment, meaning that some of the assumption is not true.

The discrepancy comes from boundary condition. The heat diffuses about μm for 1 ns on graphene, which is on par with the size of Quantifoil mesh size. Therefore, most of the heat will be absorbed by the amorphous carbon considering its gigantic mass when compared to graphene, thus preventing the sample from overheating.

Chapter 3

Corrosion inhibition of 2D materials with single-layer molecules

3.1 Motivations of corrosion inhibition

Passivation of three-dimensional (3D) materials is foundational to our civilization [68]. It is becoming increasingly critical to facilely passivate emerging 2D materials such as transition metal dichalcogenides (TMDs), black phosphorous (BP), silicene, stanene [69–72], etc., which are highly susceptible to corrosion under ambient conditions with water, air, or even small amounts of acidic or basic contaminants [17, 70, 71, 73], while retaining these 2D materials’ intrinsic properties for device applications. In the materials processing context, it might also be useful to be able to selectively take off the protection monolayer reversibly for patterning with ultra-high spatial resolution.

Several passivation strategies have been developed for 2D materials including covering by more robust 2D materials such as graphene [74] and hexagonal boron nitride (hBN) [75]. They suffer, however, from processability issues and other drawbacks: metal oxide coatings are prone to cracking and are less deformable [76, 77], polymers (e.g. poly(methyl methacrylate) (PMMA), polystyrene (PS), Parylene, perylene-3,4,9,10-tetracarboxylic dianhydride (PTCDA) are readily attacked by organic solvents and offer limited durability [73, 78–80], while self-assembled monolayers (SAMs) with silane-terminated octadecyltrichlorosilane (OTS) [81] are very toxic. Here, we

discovered a simple and scalable process for passivating a large variety of 2D materials that greatly increases their lifetime under ambient or even harsh chemical and thermal conditions. It involves coating ~ 1 nm-thick monolayers of linear alkylamines onto the surface of 2D materials. The coatings can be removed, refreshing the surface of 2D materials. Molecular dynamics simulations suggest that the alkylamine coatings repel H_2O but are permeable to O_2 , which reacts with the 2D material to form an ultra-thin oxide passivation layer beneath the alkylamine that grows very slowly. Normally soluble in water, this oxide layer is protected from dissolution by the hydrophobic alkylamine molecule coating above, which shuts down subsequent cycles of oxidation/dissolution, leading to significantly slower corrosion and longevity for many different classes of 2D crystals.

3.2 One-pot method for hexylamine deposition

In our experiment [82], *n*-hexylamine (Sigma-Aldrich, 99%) was degassed with freeze-pump-thaw method for 3 cycles, dried by activated 4 Å molecular sieves for 3 days, and kept in an argon-filled glove box with O_2 and H_2O levels lower than 0.1 ppm. The two dimensional (2D) crystals are mechanically exfoliated and transferred or directly chemical vapor deposition (CVD) onto a piece of silicon wafer (with a 190 nm SiO_2 surface layer), denoted as 2D/ SiO_2 /Si, after SiO_2 /Si substrates were washed in water, isopropyl alcohol (IPA) and acetone, respectively, by sonication for 10 mins, followed by the annealing in air for 30 min at 200 °C to remove the absorbed water on surface. The exfoliation was done with Scotch Tape in a glove box for BP, but in the air for other four 2D materials: MoTe_2 , WTe_2 , WSe_2 , TaS_2 , and NbSe_2 . In the following, coating of *n*-hexylamine onto BP is taken as the example to introduce the whole coating procedure.

The whole coating process can be divided into two steps, which is performed in the Acrylic glove box, as schematically explained in the Figure 3-1(A-C). Such glove box can maintain a certain level (~ 30 ppm) O_2 and H_2O , which is necessary for uniform oxidation and hydroxylation of BP surface layer during amine growth. In

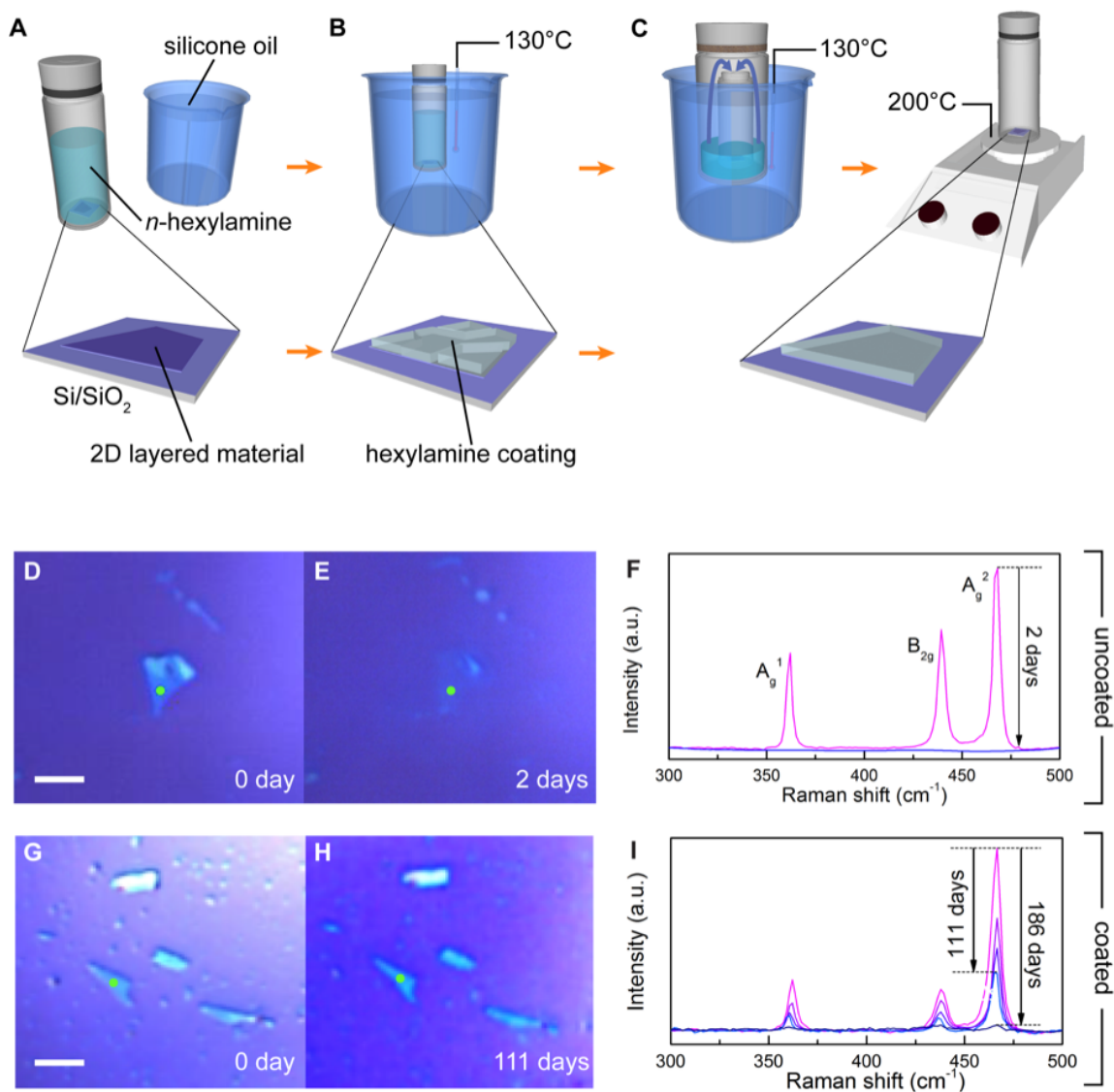


Figure 3-1: Coating *n*-hexylamine on BP flakes and aging test with Raman spectroscopy.

brief, 2D/SiO₂/Si samples were completely immersed in excess amount (2-10 mL, depending on the size of reactor vial or petri dish) of *n*-hexylamine contained in a glass vial or petri-dish, covered with a cap. Such vial or petri-dish based reactor was immersed into a silicone oil bath or sitting on a hotplate which will be heated up for the first step growth. This step growth was maintained about 20 min at 130 °C and then cooled down to room temperature (RT) and kept for half an hour to complete the first step growth. After this, samples were taken out and rinsed with hexane to

remove the attached amine residues. For the second step growth, the samples under heating at 130°C will be steamed in the amine vapor for about 20 min, with the subsequent cooling down to RT for another half an hour. After gently rinsed with hexane and dried, the samples were transferred to another glove box with low O₂ and H₂O levels (< 0.1 ppm) to be sealed in a glass vial for the final simple post-growth annealing at 200 °C for 30 min. After cooling down, the sample was then ready for characterization and testing. It is worth noting here, on the other hand, if the two-step reaction environment is in a pure argon environment, i.e. with the O₂ and H₂O levels < 0.1 ppm, a proper amount of deionized water is necessary to be added into the alkylamine for the coating. Typically, the workable volume ratio of water to liquid alkylamine (H₂O/alkylamine) is in the range of 10⁻⁴ – 10⁻³.

From the beginning, *n*-hexylamine coating parameters were optimized step by step based on BP. After that, the similar parameters after optimization will be applied for *n*-hexylamine coating onto other 2D materials (Table 3.2), and other amine molecules with different carbon chain lengths onto BP (Table 3.1).

Since BP is the most vulnerable to corrosion among the 2D materials studied in this work, it creates the most problematic challenges for processing and applications. It is used here as an illustrative example of our corrosion inhibitors. Once mechanically exfoliated, the BP flakes are highly reactive and chemically unstable. After keeping a ~3 nm-thick BP flake (Figure 3-1(D)) in ambient air for 2 days, only vague traces remain (Figure 3-1(E)), even when care is taken to prevent light exposure, known to accelerate the damage. As shown in Figure 3-1(F), the three characteristic Raman peaks of BP at 361 cm⁻¹ (A_g¹), 438 cm⁻¹ (B_{2g}), and 466 cm⁻¹ (A_g²) completely disappear after 2 days (Figure 3-1(F)). The degradation of BP was further expedited when exposed to light. This is in line with previous reports⁹ which showed that the lifetime of BP (defined as the time needed for the Raman intensity to drop to e⁻¹ of its original) is $\tau \approx 1$ hour when a 2.8 nm-thick sample is exposed to a photon flux of 1.8×10^3 W/cm², and $\tau \approx 10$ minutes when exposed to a photon flux of 1.7×10^4 W/cm².

In contrast, *n*-hexylamine protected BP (HA-BP hereafter) exhibits robust BP

characteristics for a significantly extended period. The difference in optical images for HA-BP between 0 day and 111 days is essentially indiscernible except for a slight edge corrosion (Figure 3-1(G, H)); 32% of the intensity of A_g^2 was retained after 111 days (Figure 3-1(I)). The light flux from laser and lamp absorbed by HA-BP during Raman measurements in 111 days is equivalent to 1.0×10^5 W/cm² for ~ 2 hours in total. Since this photon exposure is already substantial to cause the degradation of bare BP (from ref. [70], and can also be seen from the dark laser spot in Figure 3-1(H)), we conclude that the lifetime of HA-BP can be extended even further if the sample were not exposed to the strong laser.

Our coating process involves first the hydroxylation of BP and then proton transfer to the -NH₂ group of *n*-hexylamine. Molecular simulations suggest that *n*-hexylamine forms a molecular monolayer as shown in Figure 3-2(A). The top layer of the BP surface is rapidly oxidized, presumably forming P-OH, P-O⁻, or P=O surface groups. Experimental evidences supports a model where the acidic P-OH groups on the BP surface and the terminal -NH₂ groups of alkylamines undergo a Brønsted-Lowry acid-base reaction to form a layer of alkylammonium salts that coat the BP surface through a strong electrostatic interaction with the deprotonated P-O⁻ surface sites. Confirmation that the neutral -NH₂ group in *n*-hexylamine becomes charged (i.e. -NH₃⁺) came from X-ray photoelectron spectroscopy (XPS): comparing the N 1s peaks between HA-BP, dodecylamine (C₁₂H₂₅NH₂, R-NH₂), and methylammonium chloride (CH₃NH₃Cl, R-NH₃⁺) revealed that HA-BP and R-NH₃⁺ have the same binding energy, which is blue-shifted by 2.4 eV from that of R-NH₂ Figure 3-2(B). Protonation of the terminal amine groups in our coatings is therefore unambiguous.

Inspection by atomic force microscopy (AFM) of the height profile of the same 2D flake before and after coating revealed that the *n*-hexylamine coating is around 1.5 nm thick (Figure 3-2(C)), which is consistent with the theoretical chain length of *n*-hexylamine. [83] This demonstrates that the deposition of *n*-hexylamine molecules is self-limiting. Polar organic solvents including acetone, ethanol, or isopropanol, as well as non-polar solvents like hexane, cannot remove the *n*-hexylamine coating, indicating that the interaction between *n*-hexylamine and BP is strong enough to

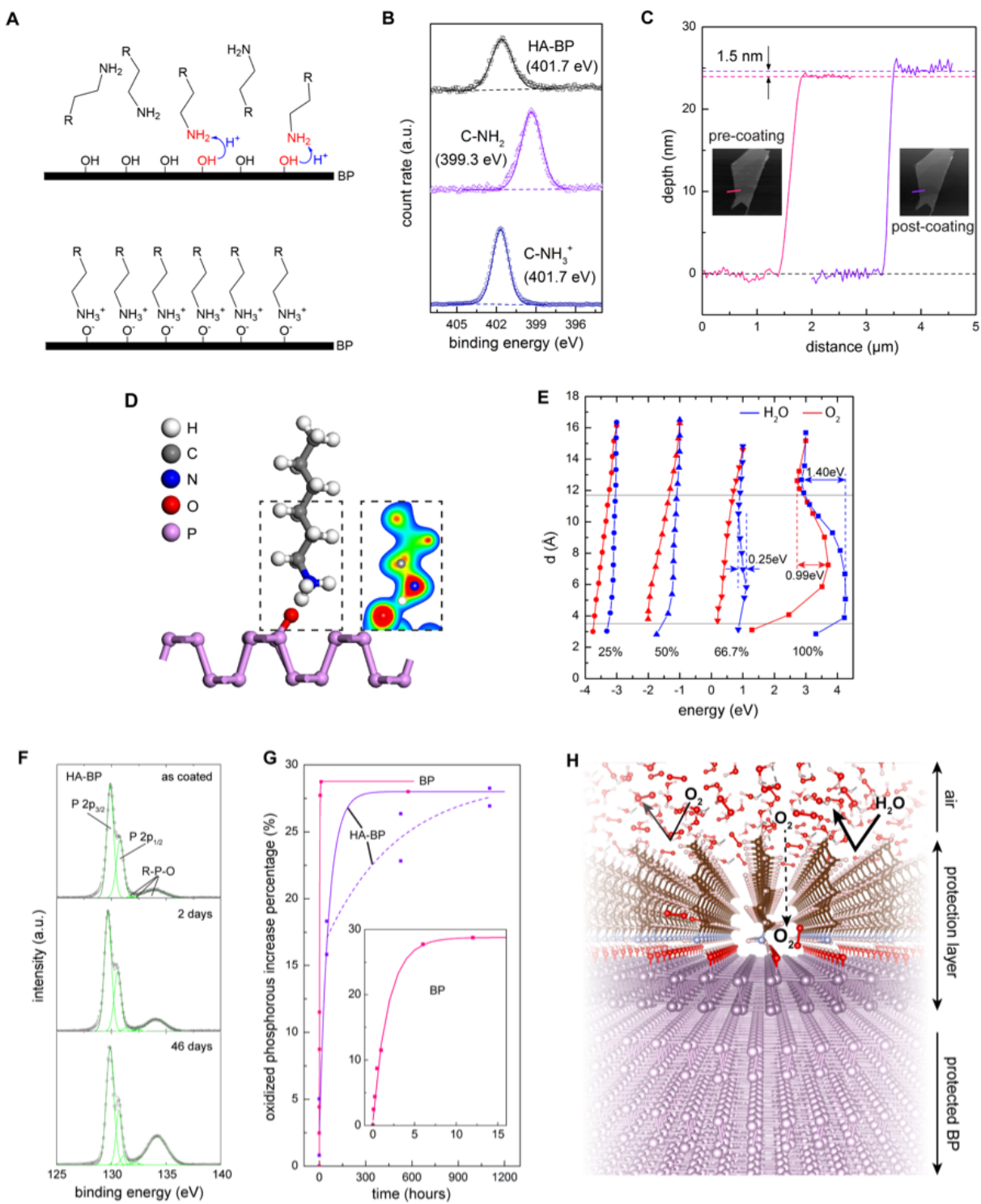


Figure 3-2: The mechanism of *n*-hexylamine coating on BP.

sustain solvent attack. We also note that *n*-hexane does not impart any corrosion protection, attesting that the amine group is key for this function and that the alkyl chain itself cannot bind strongly on BP.

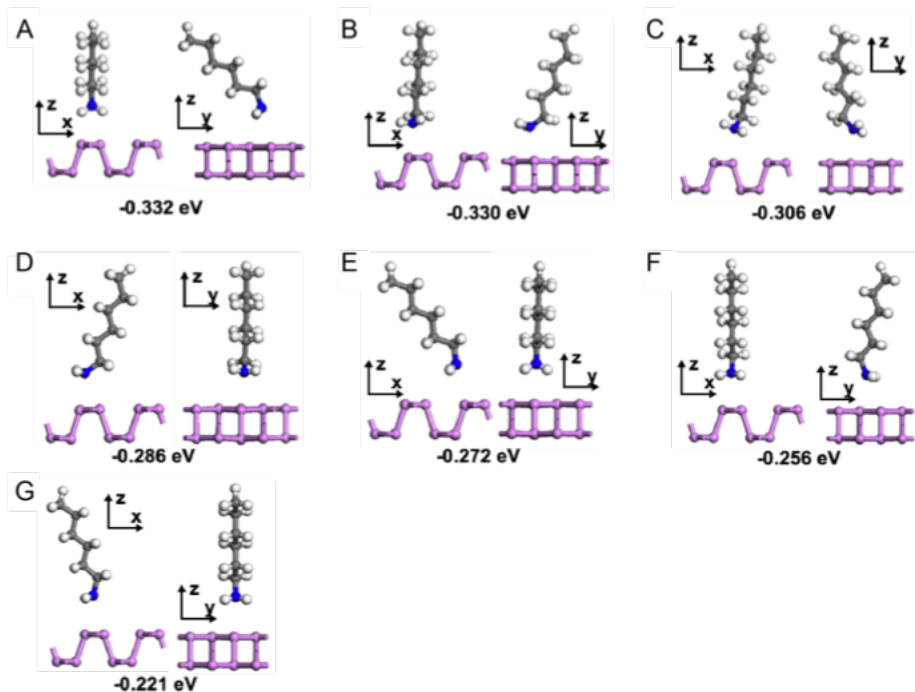


Figure 3-3: Seven different configurations for direct adsorption of *n*-hexylamine on BP. For each configuration, the front view and side view are shown, and the adsorption energy is marked under each configuration. The largest adsorption energy is only 0.33 eV.

We employed first-principles calculations to investigate the transfer of protons when *n*-hexylamine approaches P-OH (Figure 3-2(D)), formed by reacting with the water from the *n*-hexylamine coating solution. Among various structural possibilities after systematic study with results shown in Figure 3-3 to 3-6, the most likely reaction pathway agrees with the scenario ($\text{P-O}^- \text{-NH}_3^+ \text{-C}_6\text{H}_{13}$) proposed above and yields a bonding energy of 0.97 eV, which is 3-4 times stronger than the pure vdW interaction (~ 0.33 eV between *n*-hexylamine and pure BP, ~ 0.22 eV between amines and graphene [84]). The electronic density distribution shows that the H atom shares its orbital much more with N atom than with O atom (inset of Figure 3-2(D)), and a Bader's charge analysis indicates that *n*-hexylammonium ($\text{C}_6\text{H}_{13}\text{NH}_3^+$) carries a net

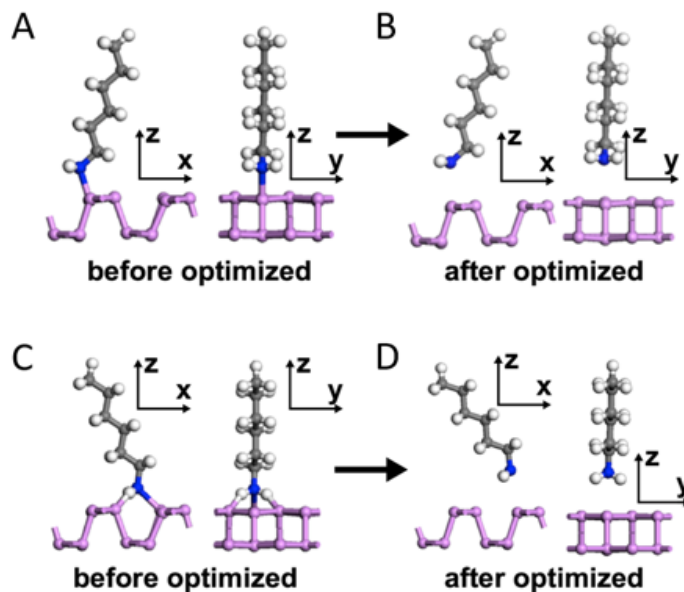


Figure 3-4: (A, C) For direct adsorption of *n*-hexylamine on BP, two special initial configurations have been tested, in which *n*-hexylamines are chemically bonded with BP. (B, D) After optimization, *n*-hexylamines in these two configurations have been repelled by BP, indicating that direct chemical bonding between *n*-hexylamines and BP is not possible.

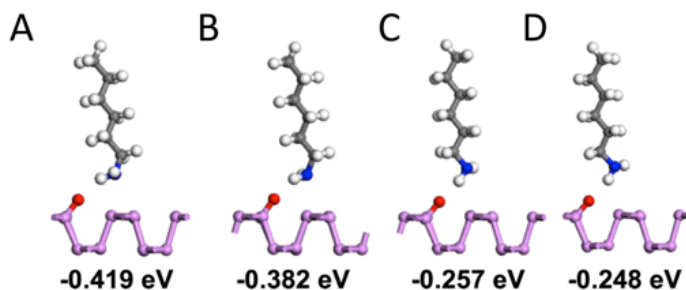


Figure 3-5: Four different configurations for adsorption of *n*-hexylamine on oxidized BP. The largest adsorption energy is 0.419 eV, indicating that oxidization of BP can enhance adsorption between BP and *n*-hexylamine.

charge of $+0.89e$, and to compensate, the rest has $-0.89e$.

In Figure 3-2(E), the migration energy barrier of H_2O penetrating through *n*-hexylamine is calculated to be 1.4 eV and O_2 1.0 eV, when *n*-hexylamine covers BP in the densest possible packing structure (hereafter defined as 100% coverage, shown in Figure 3-7); when the coverage drops to 66.7%, the migration energy barrier reduces to 0.2 eV for H_2O permeation and no barrier (0 eV) for O_2 . When the HA coverage

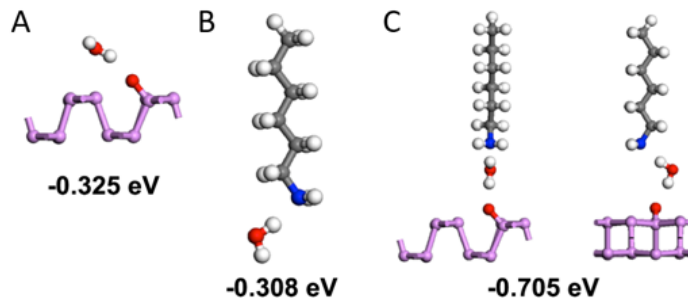


Figure 3-6: The binding energy of Various configurations when water molecule is involved.

further decreases to 50% or 25%, the migration of both H₂O and O₂ through the HA layer towards the surface of BP is barrierless.

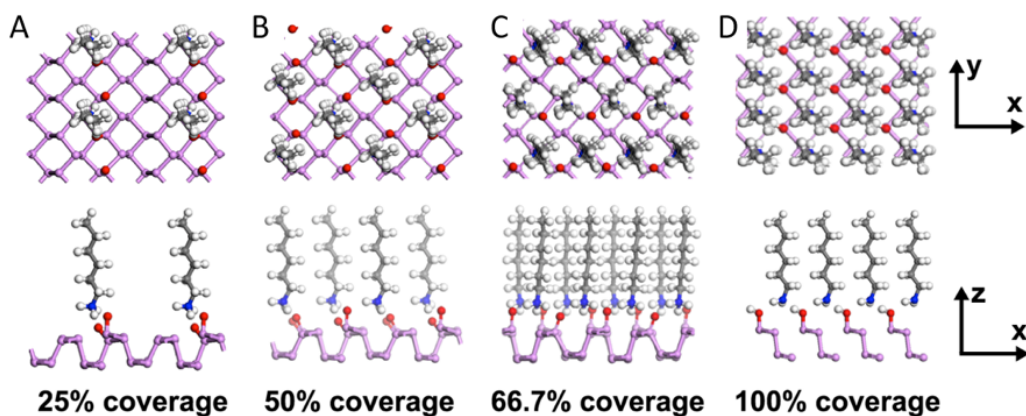


Figure 3-7: The definition of coverage on BP.

Combining this theoretical analysis with the time-evolution XPS data on phosphorous oxide concentration (Figure 3-2(F-G)), where the oxidization speed of phosphorous after *n*-hexylamine coating is significantly reduced by 32 times at the beginning of oxidation (fitting method and definition of time constant can be found in SI), we deduce the coverage density of *n*-hexylamine on BP must be more than the defined 66.7% coverage on the surface of BP.

With these conclusions, a schematic illustration of the molecular monolayer can be shown in Figure 3-2(H). The top oxidized BP layer of PO_x together with the coated *n*-hexylamine monolayer forms a dense protection layer for the BP underneath. It lowers

down the penetration speed of O₂ molecule significantly and blocks the H₂O molecule almost completely under room temperature, thus stabilizes the surface passivation layer (the oxidized BP at the top).

The anti-corrosion effect conferred by organic monolayer is not limited to *n*-hexylamine. Indeed, other linear alkylamines *n*-C_{*m*}H_{2*m*+1}NH₂ with *m* = 4 to 11, including *n*-butylamine (*n*-C₄H₉NH₂), *n*-pentylamine (*n*-C₅H₁₁NH₂), *n*-octylamine (*n*-C₈H₁₇NH₂), *n*-decylamine (*n*-C₁₀H₂₁NH₂), and *n*-undecylamine (*n*-C₁₁H₂₃NH₂), all consistently displayed similar anti-corrosion effects in ambient air. Their coatings onto BP for anti-corrosion demonstration are presented in Table 3.1, and the growth parameters for coating all these alkylamines with different carbon chain lengths are also summarized.

Table 3.1: Coating parameters for amine and hexane molecules on 2D materials, for example BP in this work.

	Boiling point (°C)	Coating temperature (°C)
<i>n</i> -C ₄ H ₉ NH ₂	~78	90
<i>n</i> -C ₅ H ₁₁ NH ₂	105	110
<i>n</i> -C ₆ H ₁₃ NH ₂	131.5	130
<i>n</i> -C ₈ H ₁₇ NH ₂	~176	140-160
<i>n</i> -C ₁₀ H ₂₁ NH ₂	~217	150-180
<i>n</i> -C ₁₁ H ₂₃ NH ₂	~240	180
C ₆ H ₅ CH ₂ NH ₂	185	180 (not protected)
<i>n</i> -C ₆ H ₁₄	68.7	80 (not protected)

3.3 Passivation Efficacy for Photodetectors

To demonstrate the passivation efficacy for actual optoelectronic devices in ambient and aggressive environments, we fabricated two BP-flakes-based photodetectors. As a direct bandgap semiconductor, with its E_{gap} continuously tunable from ~2 eV (single layer) to 0.3 eV (bulk) [85] by varying the number of layers, BP stands out as a promising material for photonic devices from near-infrared to mid-infrared. The layout of the uncoated BP detector with a channel length and width of ~3 μm and ~5

μm , respectively, between the Ti/Au electrodes is shown in Figure 3-9(A). The thickness of the BP here is 74 nm. The *n*-hexylamine-coated BP photodetector is shown in Figure 3-9(D), with comparable channel dimension and a BP thickness of 55 nm. The photocurrent as a function of input optical power under zero voltage bias (Figure 3-9(C, F), uncoated and coated respectively) was measured in ambient air with a 1550-nm laser. Both devices exhibited increased photocurrent with input power before etching (black lines labeled with pre-etching in these plots). After dipping the devices in H_2O_2 for 5 seconds and drying them subsequently, obvious degradation was observed under optical microscope on the uncoated BP device (Figure 3-9(C)), while little change was found on the coated one (Figure 3-9(F)). As evidenced by the photoelectric signal, corrosion caused severe damage to the uncoated optoelectronic device, with the photocurrent dropping to zero. In contrast, the *n*-hexylamine coated photodetector device maintained 78.6% of its original photocurrent based on the photocurrent values of $28.7 \mu\text{A}$ @post-etching and $36.5 \mu\text{A}$ @pre-etching under photoexcitation with the same input power of 3 mW. The slight drop of performance likely originates from defects in the coating layer within the boundaries between the electrode metal and the BP flake, and also likely originates from the residue of PMMA during the deposition of electrodes that blocks the growth of *n*-hexylamine.

3.4 Broad Applicability of *n*-hexylamine Coating Method

Such monolayer protection is effective not only for BP, and also for other layered 2D materials. Here for accelerated corrosion tests, we used aqueous H_2O_2 or KMnO_4 solutions as etchants. In Table 3.2, we take the optical microscopy images during the corrosion exposure for each 2D material, including BP, WS_2 , WSe_2 , $1\text{T}'\text{-MoTe}_2$, WTe_2 , TaS_2 , and NbSe_2 . It should be noted that exfoliated BP, $1\text{T}'\text{-MoTe}_2$, WTe_2 , NbSe_2 and CVD-grown single-layer WS_2 are known to be particularly susceptible to ambient corrosion, and are readily attacked by solutions of H_2O_2 . WSe_2 and TaS_2 are less vulnerable and require stronger oxidants for corrosion. A robust protection was demonstrated for *n*-hexylamine-coated 2D materials based on the sharp difference in

Table 3.2: Coating parameters optimization of n-hexylamine on BP based on the protection testing results by taking optical microscope images before and after etching/oxidation of BP flakes. The etching method with H_2O_2 (30% wt. in H_2O) etchant/oxidant follows: dip BP into H_2O_2 for 20 sec, remove BP from H_2O_2 , and leave dipped BP for 2 mins in air. Scale bars are 20 μm .

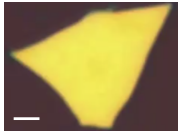
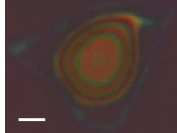
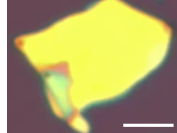
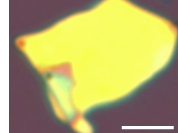
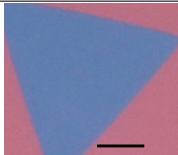
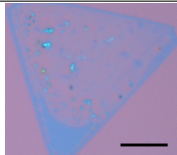
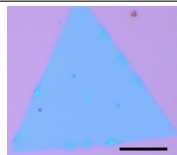
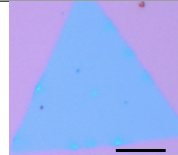
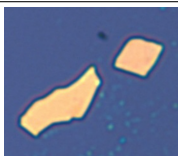
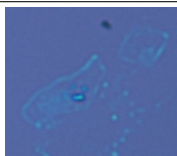
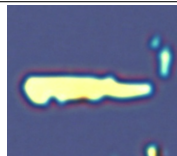
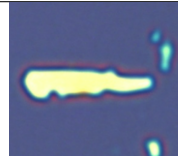
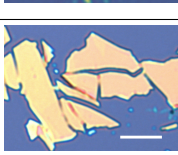
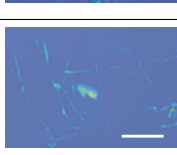
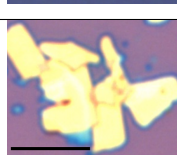
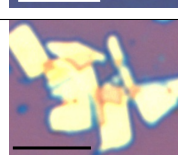




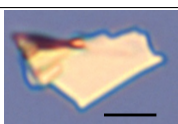
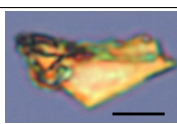
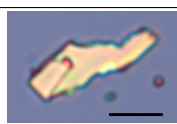
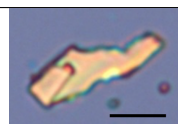
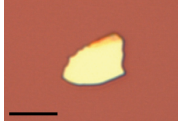
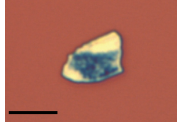
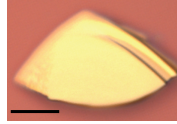
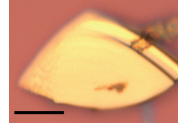
materials	bare		coated	
	before exposure	after exposure	before exposure	after exposure
BP				
WS_2				
$1\text{T}^{\prime}\text{-MoTe}_2$				
WTe_2				
WSe_2				
TaS_2				
NbSe_2				

image evolution between uncoated/unprotected and coated/protected 2D materials after their exposure to the etchants.

3.5 Reversibility of *n*-hexylamine Coating

Unlike the irreversible covalent bonding created when protecting BP with aryl diazonium precursors [86], the ionic bonding between the HA and BP is strong but still reversible. The *n*-hexylamine can be completely removed by treating HA-BP with either glacial acetic acid or a mixture of acetone and aqueous HCl (37%). Presumably, the organic-media-supported protons can penetrate the hydrophobic alkyl layer, protonate the ionized surface P-O⁻ groups, disrupting their electrostatic interaction with the alkylammonium cations. The alkylammonium cations are then released, leaving BP unprotected. This deprotection process is demonstrated in Figure 3-10, which shows that after treating HA-BP with glacial acetic acid, the newly deprotected HA-BP is indeed again susceptible to etchant. Similar demonstration is also performed for TMD flakes.

AFM data in Figure 3-11(A-C) trace the coating process on BP by monitoring flake's height and roughness. It is interesting to see two different outcomes in the different parts of sample. 1) On the left side of height profile plot, a coating layer with 1.5 nm thickness is completely removed after dipping into glacial acetic acid for 20 minutes. 2) On the right side, a coating layer with 2.0 nm thickness is first deposited, and 1.5 nm could be removed. On the other hand, in WSe₂ as presented in Figure 3-11(D-F), the tendency follows exactly the same with the second case in BP. Explanation could be as follows: 1) The first case of BP indicates that BP is actually already half oxidized before coating, so no change is observed for this part. 2) The 0.5 nm thickness increase can be explained by the oxidation of the surface layer. For this part of BP and the whole WSe₂, no oxidation occurred before coating, so an extra 0.5 nm increase is homogeneous on the whole sample. Regardless of the pre-oxidation phase, both samples restore to its initial roughness and features after uncoating process (Figure 3-11(C,F)). Similar to stainless steel (SS), the first layer of the material (e.g. BP) is turned into a passivation layer (PO_{*x*}) protecting the rest of the materials; unlike SS, the passivation layers of BP and TMDs are stabilized by *n*-hexylamine coating, preventing hydrolysis. This reversible passivation coating

is unique and unavailable from previous passivation methods of monolayer coatings. Notably, aqueous solutions of strong acids are tested to be not effective in this regard, presumably because the hydronium ion, H_3O^+ , cannot penetrate the hydrophobic alkyl layer: treating hexylamine coated samples with concentrated aqueous HCl does not remove *n*-hexylamine, which is important for device fabrication given that many wet etching processes use such strong aqueous acids. A comparison between different passivation methods are listed in the Table 3.3.

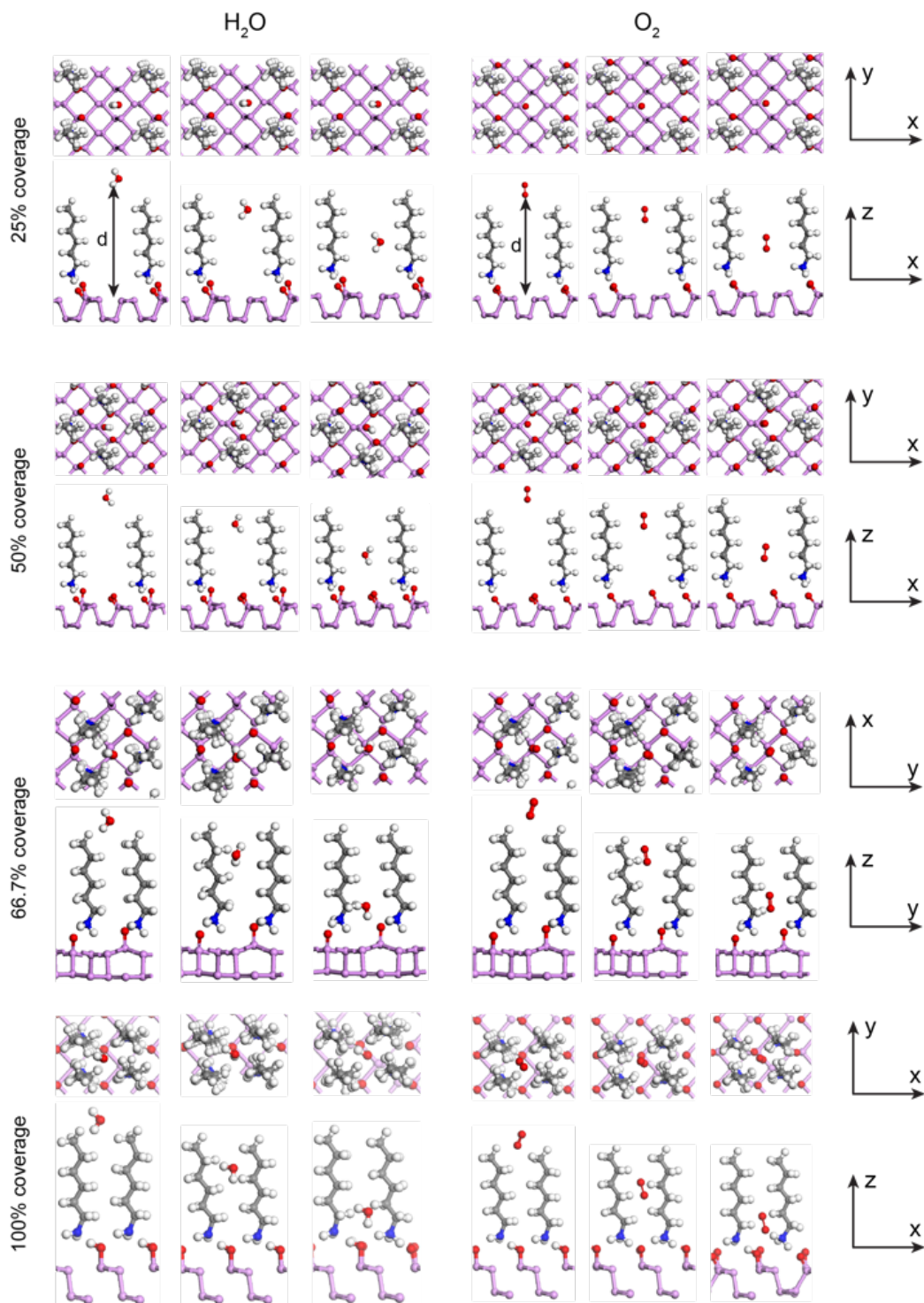


Figure 3-8: The structures of HA-BP used for calculating H_2O and O_2 molecules penetrating through the n -hexylamine coating. For each coverage and penetrating molecule type, three different locations are shown (far, middle, and close to the BP surface respectively), and each location is shown in two perspectives which are top view and side view. The distance d is defined in the first two figures of H_2O and O_2 in 25% coverage.

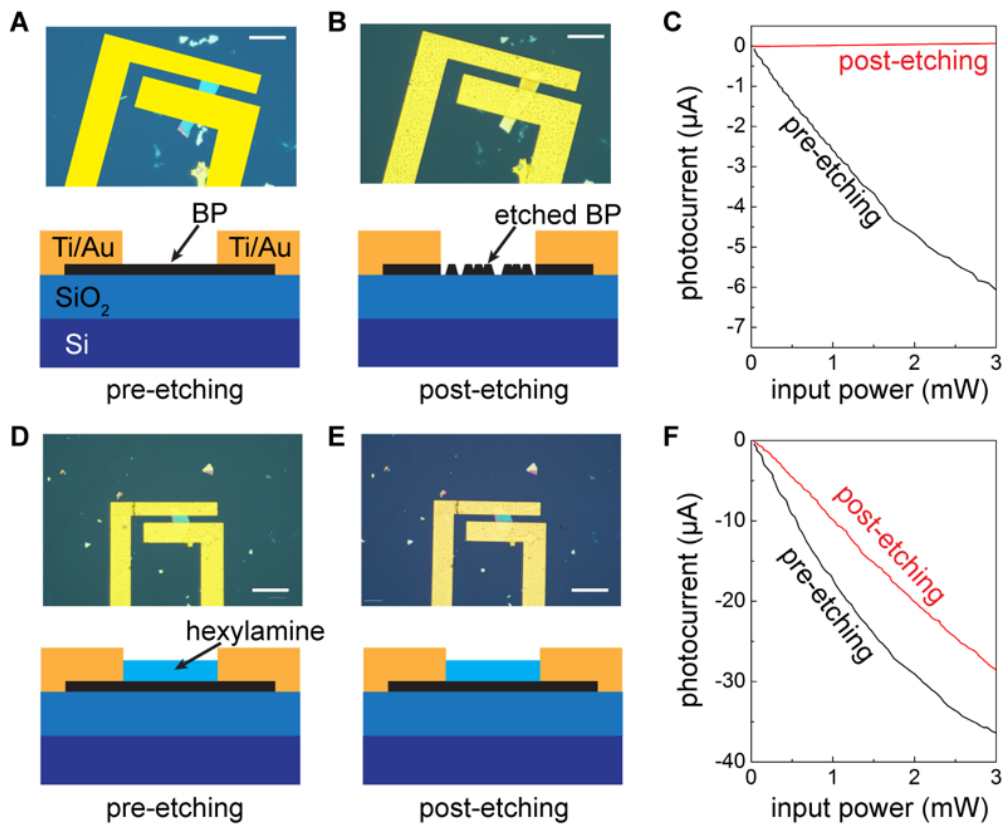


Figure 3-9: Photodetectors and etching test.

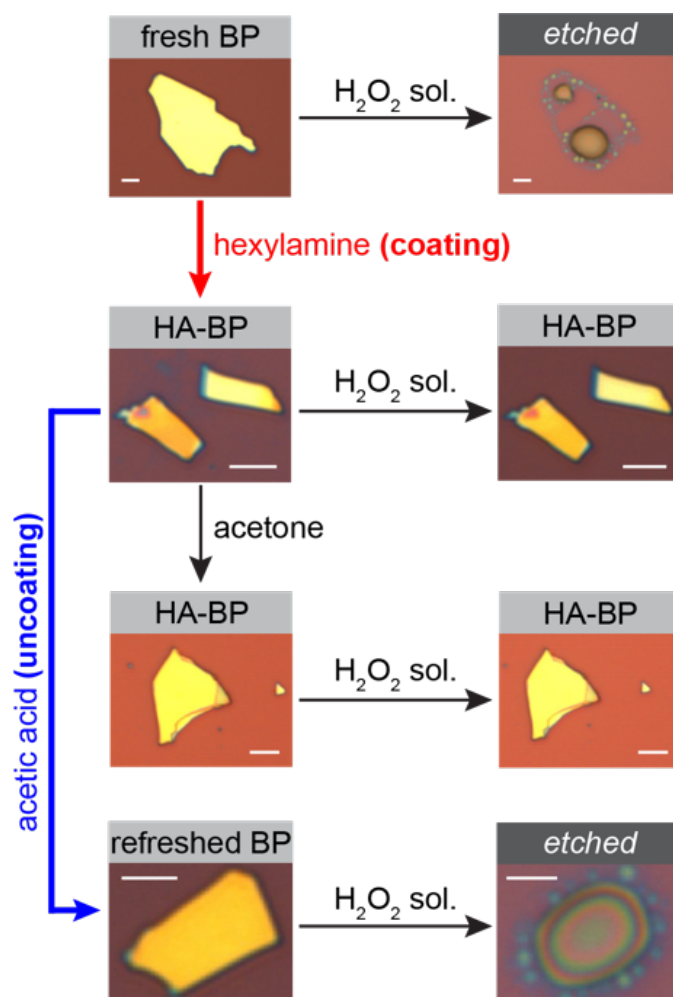


Figure 3-10: Removability of *n*-hexylamine coating on BP by organic acid.

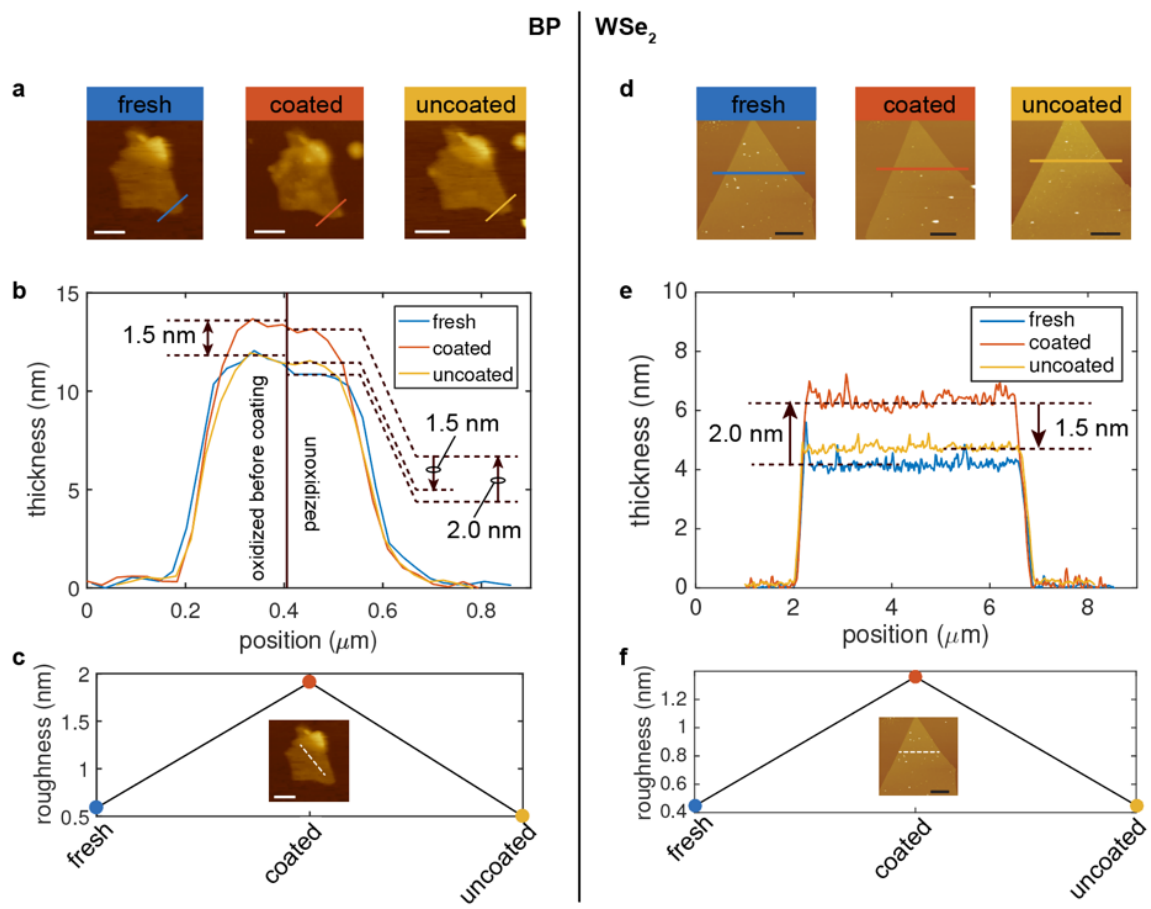


Figure 3-11: AFM data of the reversible process of *n*-hexylamine coating on BP and WSe₂.

Table 3.3: Comparison between existing protection techniques. Factors such as coating layer thickness, resistive property, and techniques used are compared.

	Thickness	Passivation Against	Susceptible to	Fabrication method	Limitations
n -hexylamine	1.5 nm	Ambient air, H ₂ O ₂ , organic solvent, bases	organic acids	solvothermal	size of container
AlO _x	2-30 nm	Ambient air, organic solvent	acids, bases, H ₂ annealing	ALD	vacuum chamber size
PMMA	100 nm	Ambient air	organic solvent, H ₂ annealing	spin coating	too thick
Graphene/hBN	4 Å	Ambient air, organic solvent, acids, bases, H ₂ annealing	-	2D materials transfer	size of 2D materials
Parylene	30-300 nm	Ambient air	-	Thermal evaporation	vacuum chamber size
Aryl-diazonium	molecular scale	Ambient air	-	wet chemistry	non-removable
ODTS	monolayer	ambient air	-	wet chemistry	processing throughput due to toxicity

3.6 Final Thoughts

Amines with low water solubility have long been known as efficient and reliable corrosion inhibitors for steels [83,87]. It is found here that it also serves as an effective coating for 2D layered materials, by blocking water for the native thin oxide layer growing at the interface between the 2D material and the alkylamine coating. The photooxidation of bare BP starts with the synergetic effect of oxygen, water and light, where phosphorous transformed to a layer of acidic phosphorus species. The thin layer of acid then coarsens into a droplet, leaving a fresh phosphorous surface in contact with ambient air, and the oxidation process starts once again [88]. *n*-hexylamine monolayer lowers the permeability of oxygen and strongly blocks the water molecules from directly contacting the oxide passivation layer and phosphorous. Although the first BP layer is still oxidized by O₂, it is isolated from ambient humidity by the hydrophobic alkyl monolayer, which prevents the water from dissolving this top native oxide that would have perpetuated the corrosion. Our experimental finding of the passivation effect on BP is consistent with the theoretical prediction that mere BP + O₂ reaction forming BP-PO_x should be fully stable and self-limiting at ~1-2 nm if no moisture exists [89].

In summary, in this chapter, we have developed a strategy to effectively slow down the corrosion of BP by coating of alkylamine monolayer onto its surface. General applicability on a variety of other layered materials is also demonstrated. The alkylamine monolayer is robust in a range of chemical and thermal environments, including ambient air. The facile coating method can be implemented with many different substrates and is compatible with all linear alkylamines no shorter than *n*-butylamine, thus offering a platform for controlling the surface physics and chemistry of a rich tableau of 2D materials. Because of its simplicity, eco-friendliness and low cost, we envision it to be scalable and adaptable in various industrial configurations.

Chapter 4

The Future of Atomic Engineering

One of the biggest obstacles of Atomic Engineering is to upscale the atomic foundry process. To achieve this, automatic atom-control protocol is necessary to be developed as a computer program. The separation of two steps in PKS theory bestows researchers with the advantage of building a database of outcome functions for different configurations *a priori*. The very basic step of Atomic Engineering inside STEM may then be decomposed into the following procedures (Figure 4-1):

1. Obtain atomic-resolved images of the target crystal structure (STEM).
2. Parse the crystal information with a standard data structure (either by cross correlation method or by machine learning in computer). This is the input of the following step.
3. Search for the outcome functions in the pre-computed database of different configurations. The output becomes the input the following step.
4. With the basic information retrieved from STEM (e.g. electron energy, temperature, gas environment, etc.) combined with the outcome functions, PKS theory outputs an optimized set of tunable parameters.
5. The parameter set is sent back to STEM to control the atom.

Another possible advancement comes from the instrument, where multiple electron-beams, with one being high energy (used for modifying atomic structure) and another

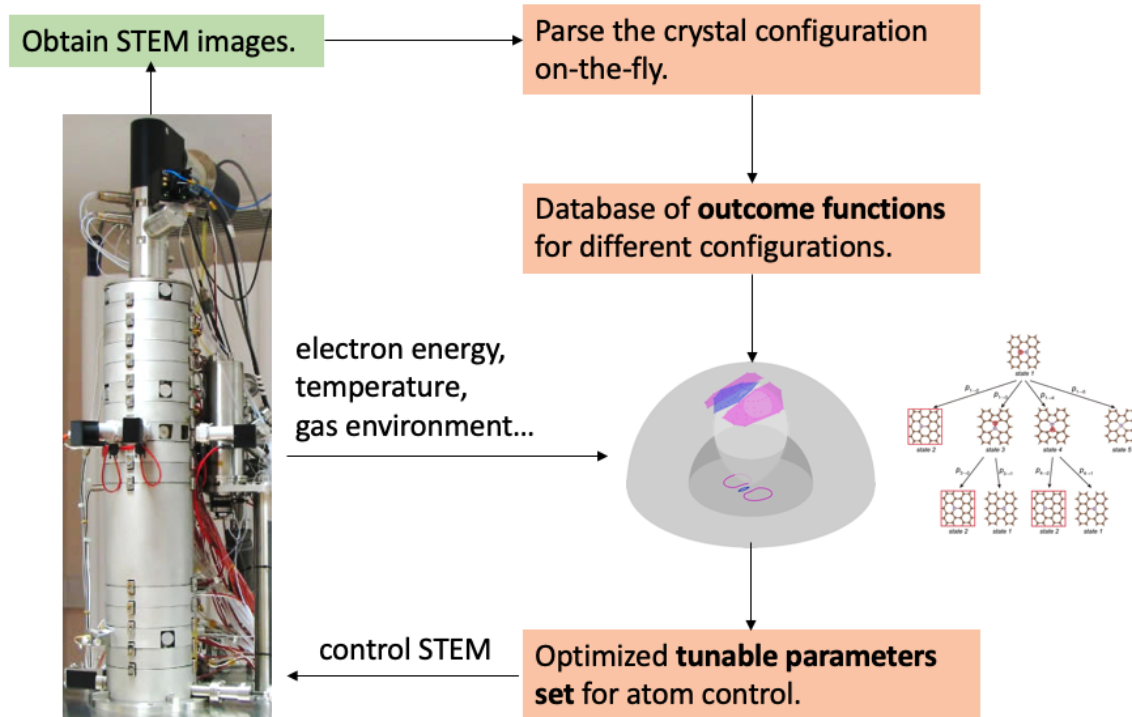


Figure 4-1: The flow chart of one single step in Atomic Engineering with automatic image recognition and control feedback. The core of control strategy is determined by PKS theory developed in Chapter 3. Image credit: Nion.

being low energy (used for imaging without messing up the atomic structure), are very much desired to get incorporated into the whole STEM system. Right now, the cost of R&D and the low market demand for such a system may stagnate the development process for such a dual-beam system. However, I envision that the future atomic engineering will always equip several set of systems to decouple the functional purpose and avoid unnecessary damage that might be incurred.

High energy electron beam, compared with STM, also pertains the advantage of being able to penetrate through thin samples and acquire confocal images on different layers. By harnessing the z-dimension, Atomic Engineering can be extended to 3D system by stacking a pile of 2D materials. A schematic breakdown of the layered materials are shown in Figure 4-2.

Even though atomic engineering might take a long way to get scaled up, a-few-atom controllability is already significant in the fields like quantum engineering, where

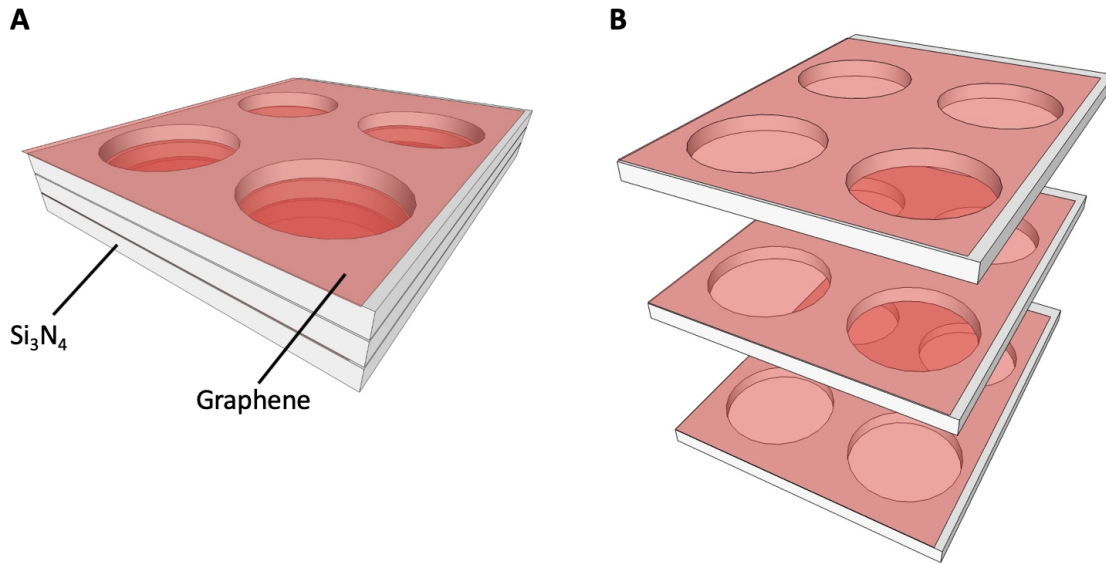


Figure 4-2: The stacked structure of 2D materials. With the capability of penetrating through thin layers with little degradation of electron beam wave front, focused electron beams can be used for controlling atoms on different layers and harnessing the z-dimension.

defects on the scale of a single atom is found to be usable as color center for quantum information storage [90, 91]. With the capability of controlling atoms on the scale of a thousand with high precision, Atomic Engineering can open up new venues for materials fabrication and physics.

Bibliography

- [1] T. Von Kármán, “Atomic engineering?,” *Journal of Applied Physics*, vol. 17, no. 1, pp. 2–3, 1946.
- [2] G. E. Moore *et al.*, “Cramming more components onto integrated circuits,” 1965.
- [3] T. Simonite, “Moore’s law is dead. now what,” *MIT Technology Review*, 2016.
- [4] D. M. Eigler and E. K. Schweizer, “Positioning single atoms with a scanning tunnelling microscope,” *Nature*, vol. 344, no. 6266, p. 524, 1990.
- [5] D. . M. Eigler, C. Lutz, and W. Rudge, “An atomic switch realized with the scanning tunnelling microscope,” *Nature*, vol. 352, no. 6336, p. 600, 1991.
- [6] O. Custance, R. Perez, and S. Morita, “Atomic force microscopy as a tool for atom manipulation,” *Nature nanotechnology*, vol. 4, no. 12, p. 803, 2009.
- [7] O. Scherzer, “Über einige fehler von elektronenlinsen,” *Zeitschrift für Physik*, vol. 101, no. 9-10, pp. 593–603, 1936.
- [8] W. Zhou, M. D. Kapetanakis, M. P. Prange, S. T. Pantelides, S. J. Pennycook, and J.-C. Idrobo, “Direct determination of the chemical bonding of individual impurities in graphene,” *Physical review letters*, vol. 109, no. 20, p. 206803, 2012.
- [9] Q. M. Ramasse, C. R. Seabourne, D.-M. Kepaptsoglou, R. Zan, U. Bangert, and A. J. Scott, “Probing the bonding and electronic structure of single atom dopants in graphene with electron energy loss spectroscopy,” *Nano letters*, vol. 13, no. 10, pp. 4989–4995, 2013.
- [10] S. Pennycook, “Z-contrast stem for materials science,” *Ultramicroscopy*, vol. 30, no. 1-2, pp. 58–69, 1989.
- [11] O. L. Krivanek, C. Mory, M. Tence, and C. Colliex, “Eels quantification near the single-atom detection level,” *Microscopy Microanalysis Microstructures*, vol. 2, no. 2-3, pp. 257–267, 1991.
- [12] T. Susi, J. Kotakoski, D. Kepaptsoglou, C. Mangler, T. C. Lovejoy, O. L. Krivanek, R. Zan, U. Bangert, P. Ayala, J. C. Meyer, *et al.*, “Silicon–carbon bond inversions driven by 60-keV electrons in graphene,” *Physical review letters*, vol. 113, no. 11, p. 115501, 2014.

- [13] O. Dyck, S. Kim, S. V. Kalinin, and S. Jesse, “Placing single atoms in graphene with a scanning transmission electron microscope,” *Applied Physics Letters*, vol. 111, no. 11, p. 113104, 2017.
- [14] U. Dürig, O. Züger, and D. Pohl, “Observation of metallic adhesion using the scanning tunneling microscope,” *Physical review letters*, vol. 65, no. 3, p. 349, 1990.
- [15] C. Su, M. Tripathi, Q.-B. Yan, Z. Wang, Z. Zhang, C. Hofer, H. Wang, L. Basile, G. Su, M. Dong, *et al.*, “Engineering single-atom dynamics with electron irradiation,” *Science advances*, vol. 5, no. 5, p. eaav2252, 2019.
- [16] T. Susi, J. Kotakoski, R. Arenal, S. Kurasch, H. Jiang, V. Skakalova, O. Stephan, A. V. Krashennnikov, E. I. Kauppinen, U. Kaiser, *et al.*, “Atomistic description of electron beam damage in nitrogen-doped graphene and single-walled carbon nanotubes,” *ACS nano*, vol. 6, no. 10, pp. 8837–8846, 2012.
- [17] A. K. Geim and I. V. Grigorieva, “Van der waals heterostructures,” *Nature*, vol. 499, no. 7459, p. 419, 2013.
- [18] K. F. Mak, C. Lee, J. Hone, J. Shan, and T. F. Heinz, “Atomically thin mos 2: a new direct-gap semiconductor,” *Physical review letters*, vol. 105, no. 13, p. 136805, 2010.
- [19] H. R. Gutiérrez, N. Perea-López, A. L. Elías, A. Berkdemir, B. Wang, R. Lv, F. López-Uriás, V. H. Crespi, H. Terrones, and M. Terrones, “Extraordinary room-temperature photoluminescence in triangular ws₂ monolayers,” *Nano letters*, vol. 13, no. 8, pp. 3447–3454, 2012.
- [20] Y. Zhang, T.-R. Chang, B. Zhou, Y.-T. Cui, H. Yan, Z. Liu, F. Schmitt, J. Lee, R. Moore, Y. Chen, *et al.*, “Direct observation of the transition from indirect to direct bandgap in atomically thin epitaxial mose 2,” *Nature nanotechnology*, vol. 9, no. 2, p. 111, 2014.
- [21] J. S. Ross, P. Klement, A. M. Jones, N. J. Ghimire, J. Yan, D. Mandrus, T. Taniguchi, K. Watanabe, K. Kitamura, W. Yao, *et al.*, “Electrically tunable excitonic light-emitting diodes based on monolayer wse 2 p–n junctions,” *Nature nanotechnology*, vol. 9, no. 4, p. 268, 2014.
- [22] X. Qian, J. Liu, L. Fu, and J. Li, “Quantum spin hall effect in two-dimensional transition metal dichalcogenides,” *Science*, vol. 346, no. 6215, pp. 1344–1347, 2014.
- [23] Y. Yu, F. Yang, X. F. Lu, Y. J. Yan, Y.-H. Cho, L. Ma, X. Niu, S. Kim, Y.-W. Son, D. Feng, *et al.*, “Gate-tunable phase transitions in thin flakes of 1t-tas 2,” *Nature nanotechnology*, vol. 10, no. 3, p. 270, 2015.
- [24] G. E. Moore, “Cramming more components onto integrated circuits,” *Proceedings of the IEEE*, vol. 86, no. 1, pp. 82–85, 1998.

- [25] M. Plumer, J. Van Ek, and W. Cain, “New Paradigms in Magnetic Recording,” *La Physique au Canada*, vol. 67, no. 1, pp. 3353–3355, 2011.
- [26] J. Kotakoski, C. Mangler, and J. C. Meyer, “Imaging atomic-level random walk of a point defect in graphene,” *Nature communications*, vol. 5, p. 3991, 2014.
- [27] R. Ishikawa, R. Mishra, A. R. Lupini, S. D. Findlay, T. Taniguchi, S. T. Pantelides, and S. J. Pennycook, “Direct observation of dopant atom diffusion in a bulk semiconductor crystal enhanced by a large size mismatch,” *Physical review letters*, vol. 113, no. 15, p. 155501, 2014.
- [28] J. Lee, W. Zhou, S. J. Pennycook, J.-C. Idrobo, and S. T. Pantelides, “Direct visualization of reversible dynamics in a si 6 cluster embedded in a graphene pore,” *Nature communications*, vol. 4, p. 1650, 2013.
- [29] T. Susi, D. Kepaptsoglou, Y.-C. Lin, Q. M. Ramasse, J. C. Meyer, K. Suenaga, and J. Kotakoski, “Towards atomically precise manipulation of 2d nanostructures in the electron microscope,” *2D Materials*, vol. 4, no. 4, p. 042004, 2017.
- [30] C. Su, H. Jiang, and J. Feng, “Two-dimensional carbon allotrope with strong electronic anisotropy,” *Physical Review B*, vol. 87, no. 7, p. 075453, 2013.
- [31] P. A. Denis, “Band gap opening of monolayer and bilayer graphene doped with aluminium, silicon, phosphorus, and sulfur,” *Chemical Physics Letters*, vol. 492, no. 4-6, pp. 251–257, 2010.
- [32] A. Ajoy, U. Bissbort, M. D. Lukin, R. L. Walsworth, and P. Cappellaro, “Atomic-scale nuclear spin imaging using quantum-assisted sensors in diamond,” *Physical Review X*, vol. 5, no. 1, p. 011001, 2015.
- [33] D. K. Schweizer and E. K. Eigler, “Positioning single atoms with a scanning tunneling microscope,” *Nature*, vol. 344, pp. 524–525, 1990.
- [34] F. Kalff, M. P. Rebergen, E. Fahrenfort, J. Girovsky, R. Toskovic, J. L. Lado, J. Fernández-Rossier, and A. F. Otte, “A kilobyte rewritable atomic memory,” *Nature nanotechnology*, vol. 11, no. 11, p. 926, 2016.
- [35] K. Suenaga and M. Koshino, “Atom-by-atom spectroscopy at graphene edge,” *Nature*, vol. 468, no. 7327, p. 1088, 2010.
- [36] O. L. Krivanek, M. F. Chisholm, V. Nicolosi, T. J. Pennycook, G. J. Corbin, N. Dellby, M. F. Murfitt, C. S. Own, Z. S. Szilagy, M. P. Oxley, *et al.*, “Atom-by-atom structural and chemical analysis by annular dark-field electron microscopy,” *Nature*, vol. 464, no. 7288, p. 571, 2010.
- [37] R. J. Nicholls, A. T. Murdock, J. Tsang, J. Britton, T. J. Pennycook, A. Koós, P. D. Nellist, N. Grobert, and J. R. Yates, “Probing the bonding in nitrogen-doped graphene using electron energy loss spectroscopy,” *ACS nano*, vol. 7, no. 8, pp. 7145–7150, 2013.

- [38] U. Bangert, W. Pierce, D. Kepaptsoglou, Q. Ramasse, R. Zan, M. Gass, J. Van den Berg, C. Boothroyd, J. Amani, and H. Hofsass, "Ion implantation of graphene toward ic compatible technologies," *Nano Letters*, vol. 13, no. 10, pp. 4902–4907, 2013.
- [39] T. Susi, T. P. Hardcastle, H. Hofsäss, A. Mittelberger, T. J. Pennycook, C. Mangler, R. Drummond-Brydson, A. J. Scott, J. C. Meyer, and J. Kotakoski, "Single-atom spectroscopy of phosphorus dopants implanted into graphene," *2D Materials*, vol. 4, no. 2, p. 021013, 2017.
- [40] D. Kepaptsoglou, T. P. Hardcastle, C. R. Seabourne, U. Bangert, R. Zan, J. A. Amani, H. Hofsäss, R. J. Nicholls, R. M. Brydson, A. J. Scott, *et al.*, "Electronic structure modification of ion implanted graphene: the spectroscopic signatures of p-and n-type doping," *ACS nano*, vol. 9, no. 11, pp. 11398–11407, 2015.
- [41] T. Susi, J. C. Meyer, and J. Kotakoski, "Manipulating low-dimensional materials down to the level of single atoms with electron irradiation," *Ultramicroscopy*, vol. 180, pp. 163–172, 2017.
- [42] T. Susi, J. Kotakoski, D. Kepaptsoglou, T. C. Lovejoy, O. L. Krivanek, and R. Zan, "Silicon-carbon bond inversions driven by 60 keV electrons in graphene," *arXiv*, pp. 1–21, 2014.
- [43] M. Tripathi, A. Mittelberger, N. A. Pike, C. Mangler, J. C. Meyer, M. J. Verstraete, J. Kotakoski, and T. Susi, "Electron-beam manipulation of silicon dopants in graphene," *Nano letters*, vol. 18, no. 8, pp. 5319–5323, 2018.
- [44] B. M. Hudak, J. Song, H. Sims, M. C. Tropicovsky, T. S. Humble, S. T. Pantelides, P. C. Snijders, and A. R. Lupini, "Directed atom-by-atom assembly of dopants in silicon," *ACS nano*, vol. 12, no. 6, pp. 5873–5879, 2018.
- [45] A. Zobelli, A. Gloter, C. Ewels, G. Seifert, and C. Colliex, "Electron knock-on cross section of carbon and boron nitride nanotubes," *Physical Review B*, vol. 75, no. 24, p. 245402, 2007.
- [46] J. Kotakoski, J. Meyer, S. Kurasch, D. Santos-Cottin, U. Kaiser, and A. Krasheninnikov, "Stone-wales-type transformations in carbon nanostructures driven by electron irradiation," *Physical Review B*, vol. 83, no. 24, p. 245420, 2011.
- [47] T. Susi, C. Hofer, G. Argentero, G. T. Leuthner, T. J. Pennycook, C. Mangler, J. C. Meyer, and J. Kotakoski, "Isotope analysis in the transmission electron microscope," *Nature communications*, vol. 7, p. 13040, 2016.
- [48] C. H. Lui, K. F. Mak, J. Shan, T. F. Heinz, *et al.*, "Ultrafast photoluminescence from graphene," *Physical Review Letters*, vol. 105, no. 12, p. 127404, 2010.

- [49] R. Zan, Q. M. Ramasse, U. Bangert, and K. S. Novoselov, “Graphene reknits its holes,” *Nano Letters*, vol. 12, pp. 3936–3940, 2012.
- [50] R. Egerton, “Beam-induced motion of adatoms in the transmission electron microscope,” *Microscopy and Microanalysis*, vol. 19, no. 2, pp. 479–486, 2013.
- [51] J. C. Idrobo, C. Su, J. Li, and J. Kong, “Revealing the bonding of nitrogen impurities in monolayer graphene,” *Microscopy and Microanalysis*, vol. 23, no. S1, pp. 1750–1751, 2017.
- [52] J. Ma, D. Alfè, A. Michaelides, and E. Wang, “Stone-wales defects in graphene and other planar sp²-bonded materials,” *Physical Review B*, vol. 80, no. 3, p. 033407, 2009.
- [53] W. A. McKinley Jr and H. Feshbach, “The coulomb scattering of relativistic electrons by nuclei,” *Physical Review*, vol. 74, no. 12, p. 1759, 1948.
- [54] J. C. Meyer, F. Eder, S. Kurasch, V. Skakalova, J. Kotakoski, H. J. Park, S. Roth, A. Chuvilin, S. Eychen, G. Benner, A. V. Krasheninnikov, and U. Kaiser, “Accurate measurement of electron beam induced displacement cross sections for single-layer graphene,” *Physical Review Letters*, vol. 108, no. May, pp. 1–6, 2012.
- [55] A. I. Chirita, T. Susi, and J. Kotakoski, “Influence of temperature on the displacement threshold energy in graphene,” *arXiv preprint arXiv:1811.04011*, 2018.
- [56] J. Kotakoski, C. Jin, O. Lehtinen, K. Suenaga, and A. Krasheninnikov, “Electron knock-on damage in hexagonal boron nitride monolayers,” *Physical Review B*, vol. 82, no. 11, p. 113404, 2010.
- [57] Z. Shi, E. Tsymbalov, M. Dao, S. Suresh, A. Shapeev, and J. Li, “Deep elastic strain engineering of bandgap through machine learning,” *Proceedings of the National Academy of Sciences*, vol. 116, no. 10, pp. 4117–4122, 2019.
- [58] M. Grüning, O. Gritsenko, and E. Baerends, “Exchange-correlation energy and potential as approximate functionals of occupied and virtual kohn–sham orbitals: Application to dissociating h₂,” *The Journal of chemical physics*, vol. 118, no. 16, pp. 7183–7192, 2003.
- [59] G. S. Was, *Fundamentals of radiation materials science: metals and alloys*. Springer, 2016.
- [60] Hitachi Cooperation, “New coherent cold field emission source.” https://www.hitachi-hightech.com/global/science/technical/tech/microscopes/cold_fe/. Accessed 01-Sep-2019.
- [61] H. Yan, T. Low, W. Zhu, Y. Wu, M. Freitag, X. Li, F. Guinea, P. Avouris, and F. Xia, “Damping pathways of mid-infrared plasmons in graphene nanostructures,” *Nature Photonics*, vol. 7, no. 5, p. 394, 2013.

- [62] T. Susi, J. C. Meyer, and J. Kotakoski, “Quantifying transmission electron microscopy irradiation effects using two-dimensional materials,” *Nature Reviews Physics*, p. 1, 2019.
- [63] J. Li, X. Cao, T. B. Hoffman, J. H. Edgar, J. Lin, and H. Jiang, “Nature of exciton transitions in hexagonal boron nitride,” *Applied Physics Letters*, vol. 108, no. 12, p. 122101, 2016.
- [64] A. J. Giles, S. Dai, I. Vurgaftman, T. Hoffman, S. Liu, L. Lindsay, C. T. Ellis, N. Assefa, I. Chatzakis, T. L. Reinecke, *et al.*, “Ultralow-loss polaritons in isotopically pure boron nitride,” *Nature materials*, vol. 17, no. 2, p. 134, 2018.
- [65] D. Kozawa, R. Kumar, A. Carvalho, K. K. Amara, W. Zhao, S. Wang, M. Toh, R. M. Ribeiro, A. C. Neto, K. Matsuda, *et al.*, “Photocarrier relaxation pathway in two-dimensional semiconducting transition metal dichalcogenides,” *Nature communications*, vol. 5, p. 4543, 2014.
- [66] J. C. Woicik, C. Weiland, A. Rumaiz, M. Brumbach, N. Quackenbush, J. Ablett, and E. Shirley, “Revealing excitonic processes and chemical bonding in mos 2 by x-ray spectroscopy,” *Physical Review B*, vol. 98, no. 11, p. 115149, 2018.
- [67] Y. Cai, J. Lan, G. Zhang, and Y.-W. Zhang, “Lattice vibrational modes and phonon thermal conductivity of monolayer mos 2,” *Physical Review B*, vol. 89, no. 3, p. 035438, 2014.
- [68] D. D. Macdonald, “Passivity—the key to our metals-based civilization,” *Pure and Applied Chemistry*, vol. 71, no. 6, pp. 951–978, 1999.
- [69] L. Tao, E. Cinquanta, D. Chiappe, C. Grazianetti, M. Fanciulli, M. Dubey, A. Molle, and D. Akinwande, “Silicene field-effect transistors operating at room temperature,” *Nature nanotechnology*, vol. 10, no. 3, p. 227, 2015.
- [70] A. Favron, E. Gaufrès, F. Fossard, A.-L. Phaneuf-LâĂŽHeureux, N. Y. Tang, P. L. Lévesque, A. Loiseau, R. Leonelli, S. Francoeur, and R. Martel, “Photooxidation and quantum confinement effects in exfoliated black phosphorus,” *Nature materials*, vol. 14, no. 8, p. 826, 2015.
- [71] L. Li, Y. Yu, G. J. Ye, Q. Ge, X. Ou, H. Wu, D. Feng, X. H. Chen, and Y. Zhang, “Black phosphorus field-effect transistors,” *Nature nanotechnology*, vol. 9, no. 5, p. 372, 2014.
- [72] F.-f. Zhu, W.-j. Chen, Y. Xu, C.-l. Gao, D.-d. Guan, C.-h. Liu, D. Qian, S.-C. Zhang, and J.-f. Jia, “Epitaxial growth of two-dimensional stanene,” *Nature materials*, vol. 14, no. 10, p. 1020, 2015.
- [73] J. Gao, B. Li, J. Tan, P. Chow, T.-M. Lu, and N. Koratkar, “Aging of transition metal dichalcogenide monolayers,” *ACS nano*, vol. 10, no. 2, pp. 2628–2635, 2016.

- [74] M. J. Nine, M. A. Cole, D. N. Tran, and D. Losic, “Graphene: a multipurpose material for protective coatings,” *Journal of Materials Chemistry A*, vol. 3, no. 24, pp. 12580–12602, 2015.
- [75] G.-H. Lee, X. Cui, Y. D. Kim, G. Arefe, X. Zhang, C.-H. Lee, F. Ye, K. Watanabe, T. Taniguchi, P. Kim, *et al.*, “Highly stable, dual-gated mos2 transistors encapsulated by hexagonal boron nitride with gate-controllable contact, resistance, and threshold voltage,” *ACS nano*, vol. 9, no. 7, pp. 7019–7026, 2015.
- [76] J. D. Wood, S. A. Wells, D. Jariwala, K.-S. Chen, E. Cho, V. K. Sangwan, X. Liu, L. J. Lauhon, T. J. Marks, and M. C. Hersam, “Effective passivation of exfoliated black phosphorus transistors against ambient degradation,” *Nano letters*, vol. 14, no. 12, pp. 6964–6970, 2014.
- [77] H.-Y. Chang, S. Yang, J. Lee, L. Tao, W.-S. Hwang, D. Jena, N. Lu, and D. Akinwande, “High-performance, highly bendable mos2 transistors with high-k dielectrics for flexible low-power systems,” *ACS nano*, vol. 7, no. 6, pp. 5446–5452, 2013.
- [78] S. Sabri, P. Levesque, C. Aguirre, J. Guillemette, R. Martel, and T. Szkopek, “Graphene field effect transistors with parylene gate dielectric,” *Applied Physics Letters*, vol. 95, no. 24, p. 242104, 2009.
- [79] B. Chamlagain, Q. Li, N. J. Ghimire, H.-J. Chuang, M. M. Perera, H. Tu, Y. Xu, M. Pan, D. Xiaio, J. Yan, *et al.*, “Mobility improvement and temperature dependence in mose2 field-effect transistors on parylene-c substrate,” *ACS nano*, vol. 8, no. 5, pp. 5079–5088, 2014.
- [80] Y. Zhao, Q. Zhou, Q. Li, X. Yao, and J. Wang, “Passivation of black phosphorus via self-assembled organic monolayers by van der waals epitaxy,” *Advanced materials*, vol. 29, no. 6, p. 1603990, 2017.
- [81] D.-H. Kang, J. Shim, S. K. Jang, J. Jeon, M. H. Jeon, G. Y. Yeom, W.-S. Jung, Y. H. Jang, S. Lee, and J.-H. Park, “Controllable nondegenerate p-type doping of tungsten diselenide by octadecyltrichlorosilane,” *ACS nano*, vol. 9, no. 2, pp. 1099–1107, 2015.
- [82] C. Su, Z. Yin, Q.-B. Yan, Z. Wang, H. Lin, L. Sun, W. Xu, T. Yamada, X. Ji, N. Zettsu, *et al.*, “Molecular monolayer stabilizer for multilayer 2d materials,” *arXiv preprint arXiv:1906.00458*, 2019.
- [83] J. Bastidas, J. Polo, and E. Cano, “Substitutional inhibition mechanism of mild steel hydrochloric acid corrosion by hexylamine and dodecylamine,” *Journal of applied electrochemistry*, vol. 30, no. 10, pp. 1173–1177, 2000.
- [84] B. Long, M. Manning, M. Burke, B. N. Szafranek, G. Visimberga, D. Thompson, J. C. Greer, I. M. Povey, J. MacHale, G. Lejosne, *et al.*, “Non-covalent functionalization of graphene using self-assembly of alkane-amines,” *Advanced Functional Materials*, vol. 22, no. 4, pp. 717–725, 2012.

- [85] X. Ling, H. Wang, S. Huang, F. Xia, and M. S. Dresselhaus, “The renaissance of black phosphorus,” *Proceedings of the National Academy of Sciences*, vol. 112, no. 15, pp. 4523–4530, 2015.
- [86] C. R. Ryder, J. D. Wood, S. A. Wells, Y. Yang, D. Jariwala, T. J. Marks, G. C. Schatz, and M. C. Hersam, “Covalent functionalization and passivation of exfoliated black phosphorus via aryl diazonium chemistry,” *Nature chemistry*, vol. 8, no. 6, p. 597, 2016.
- [87] J. Bastidas, J. De Damborenea, A. Va, *et al.*, “Butyl substituents in n-butylamine and their influence on mild steel corrosion inhibition in hydrochloric acid,” *Journal of applied electrochemistry*, vol. 27, no. 3, pp. 345–349, 1997.
- [88] S.-L. Yau, T. P. Moffat, A. J. Bard, Z. Zhang, and M. M. Lerner, “Stm of the (010) surface of orthorhombic phosphorus,” *Chemical physics letters*, vol. 198, no. 3-4, pp. 383–388, 1992.
- [89] M. T. Edmonds, A. Tadich, A. Carvalho, A. Ziletti, K. M. O’Donnell, S. P. Koenig, D. F. Coker, B. O’Lyzilmaz, A. C. Neto, and M. Fuhrer, “Creating a stable oxide at the surface of black phosphorus,” *ACS applied materials & interfaces*, vol. 7, no. 27, pp. 14557–14562, 2015.
- [90] T. T. Tran, K. Bray, M. J. Ford, M. Toth, and I. Aharonovich, “Quantum emission from hexagonal boron nitride monolayers,” *Nature nanotechnology*, vol. 11, no. 1, p. 37, 2016.
- [91] S. A. Tawfik, S. Ali, M. Fronzi, M. Kianinia, T. T. Tran, C. Stampfl, I. Aharonovich, M. Toth, and M. J. Ford, “First-principles investigation of quantum emission from hbn defects,” *Nanoscale*, vol. 9, no. 36, pp. 13575–13582, 2017.